Dynamical polarization and plasmons in noncentrosymmetric metals

Sonu Verma, Arijit Kundu, and Tarun Kanti Ghosh
Department of Physics, Indian Institute of Technology-Kanpur, Kanpur 208 016, India

(Received 2 October 2020; revised 7 November 2020; accepted 10 November 2020; published 30 November 2020)

We study the dynamical polarization function and plasmon modes for spin-orbit coupled noncentrosymmetric metals such as $Li_2(Pd_{1-x}Pt_x)_3B$. These systems have different Fermi surface topologies for Fermi energies above and below the spin degenerate point, which is also known as the band touching point (BTP). We calculate the exact dynamical polarization function numerically and also provide its analytical expression in the long wavelength limit. We obtain the plasmon dispersion within the framework of random phase approximation. In noncentrosymmetric metals, there is a finite energy gap in between intra- and interband particle-hole continuum for vanishing excitation wave vector. In the long wavelength limit, the width of the interband particle-hole continuum behaves differently for Fermi energies below and above the BTP as a clear signature of the Fermi surface topology change. We find a single undamped optical plasmon mode lying in between the intra- and interband particle-hole continuum for Fermi energies above and below the BTP within a range of parameters. The plasmon mode below the BTP has smaller velocity than that of above the BTP. It is interesting to find that as we tune the Fermi energy around the BTP, the plasmon mode becomes damped within a range of electron-electron interaction strengths. For Fermi energies above and below the BTP, we also obtain an approximate analytical result of plasma frequency and plasmon dispersion which match well with their numerical counterparts in the long wavelength limit. The plasmon dispersion is $\propto q^2$ with q being the wave vector for plasmon excitation in the long wavelength limit. We find that varying the carrier density with fixed electron-electron interaction strength or vice versa does not change the number of undamped plasmon modes, although damped plasmon modes can be more in number for some values of these parameters. We demonstrate our results by calculating the loss function and optical conductivity, which can be measured in experiments.

DOI: 10.1103/PhysRevB.102.195208

I. INTRODUCTION

For several decades, the ubiquitous role of spin-orbit interactions [1–3] in various condensed matter systems [4–6] exhibiting exotic phenomena has been observed [7–16]. The charge carrier's spin is not a conserved quantity in spin-orbit coupled systems, which facilitate control of the spin by simple electric manipulation. The study of response functions in the presence of external perturbations in spin-orbit coupled systems with electron-electron interactions plays a vital role in understanding several fundamental many-body properties of the systems. Single-particle excitation spectra and the collective modes of the systems are determined by the dynamical response functions which incorporate the dynamical screening of Coulomb interaction [17,18], whereas the static response function governs the transport properties of the systems through the scattering by charge impurities in the presence of screened Coulomb interaction [17,18]. Also, many-body properties such as dielectric function and collective excitation spectrum of systems with spin-orbit interaction (SOI) have importance in terms of understanding the many-body correlations and observation of SOI effects in these systems [19–22,24]. Two-dimensional electron-hole gas (2DEG/2DHG) with Rashba SOI (RSOI) and Dresselhaus SOI (DSOI) in a single quantum well hosts isotropic and anisotropic plasmon spectra when considering one type of SOIs and both SOIs, respectively [22,23]. Moreover, 2DEG with RSOI in a double quantum well hosts both lower energy acoustic and optical plasmon modes with charge density oscillating out of phase and in phase in a neutralizing positive background [24].

In recent years, there have been several theoretical and experimental studies on materials showing spin-orbit interaction much higher than that of semiconductor heterostructures. Examples of such materials are three-dimensional (3D) topological insulators [25,26], Bi/Ag(111) surface alloy [27], and three-dimensional (3D) bipolar semiconductor BiTeX (X = Cl, Br, I) [28–32]. In BiTeX compounds, both in bulk and surface, the giant RSOI arises due to the local electric field as a consequence of inversion asymmetry. According to the $\mathbf{k}\cdot\mathbf{p}$ perturbation theory [29], the RSOI in these materials have a planar form like $\alpha(\boldsymbol{\sigma}\times\mathbf{k})_z$, with α being the strength of RSOI, $\boldsymbol{\sigma}$ being a vector of spin Pauli matrices, and $\mathbf{k}$ being the electron's wave vector. In addition to BiTeX compounds, B20 [33] compounds and noncentrosymmetric metals such as $Li_2(Pd_{1-x}Pt_x)_3B$ [34] also show strong RSOI due to lack of inversion symmetry. The leading-order SOI experienced by conduction electrons in these materials is described by $\alpha\boldsymbol{\sigma}\cdot\mathbf{k}$, which is quite different from the bipolar semiconductor compounds. These systems with strong RSOI possess the distinct property that the Fermi surface topology changes as one tunes the Fermi energy across the band touching point (BTP) of two

spin-split bands. It has been verified both theoretically and experimentally [35,36] that the system changes its behavior from paramagnetic to diamagnetic as Fermi energy sweeps across the BTP from below. There are also several studies in BiTeX compounds [37–49] and noncentrosymmetric metals [49–55] in the context of transport, magnetic, thermoelectric, and optical response showing distinct behavior below and above the BTP due to change in the Fermi surface topology. All these electronic properties are mainly based on the single-particle excitations of the systems. Moreover, collective modes in BiTeX compounds have been studied thoroughly [45]. The study of collective modes in noncentrosymmetric metals is still lacking. The focus of this paper is to look into several aspects of the charge collective modes of noncentrosymmetric metals by studying the full dynamical polarization function within the random phase approximation (RPA) in detail.

In this work, we calculate the dynamical polarization function (also known as Lindhard function) numerically and also provide its analytical form for small q. The spin-orbit coupled systems possess intra- and interband single particle-hole continuum (PHC). The latter is also known as *Rashba continuum*. In the long wavelength limit, the width of Rashba continuum responds to the change in the Fermi surface topology and shows different behavior for Fermi energies above and below the BTP. In noncentrosymmetric metals (NCMs), interband PHC starts at finite energy at $q = 0$. In the presence of electron-electron interaction within the framework of the jellium model, we calculate the plasmon dispersion within RPA. Due to isotropic nature of the band structure, we find a single optical undamped plasmon mode in between the intraband PHC and Rashba continuum within a range of material parameters of NCMs. In the long wavelength limit, we provide an approximate analytical formula for plasma frequency and plasmon dispersion. The plasmon dispersion is $\propto q^2$ in the long wavelength limit is similar to that of ordinary 3D electron gas [17]. The plasmon dispersion and plasma frequency extracted from both numerical and analytical results match well for small q. For Fermi energies below BTP, we find that the plasmon mode has smaller velocity than that of Fermi energies above BTP. This plasmon mode becomes damped for Fermi energies near the BTP due to the shift in the Rasbha continuum toward zero energy within a range of electron-electron interaction strengths. We also find only one single undamped plasmon mode by varying the electron-electron interaction strength, although there are more plasmon modes lying within the Rashba continuum for a range of interaction strengths for Fermi energies below and above the BTP. We calculate the loss function and optical conductivity within RPA to demonstrate the plasmon mode which can be observed in experiments.

The remainder of this paper is organized in the following manner. In Sec. II, the necessary ground-state properties of NCMs are given. In Sec. III, we discuss the intra- and interband PHC derived from the dynamical polarization function. The static Lindhard function and its singularities are also discussed. Section IV describes the plasmon dispersion in detail together with the energy loss function and optical conductivity, which can be measured experimentally. We summarize our results in Sec. V.

II. GROUND-STATE PROPERTIES

The low-energy conduction electrons in a 3D noncentrosymmetric metal can be effectively described by the following noninteracting Hamiltonian near the Γ point [33,52,56]: $H = H_0 + H_D$, where

$$H_0 = \frac{\hbar^2\mathbf{k}^2}{2m^*}\sigma_0 + \alpha\,\boldsymbol{\sigma}\cdot\mathbf{k} \tag{1}$$

and

$$H_D = \beta\left[k_x\sigma_x\left(k_y^2 - k_z^2\right) + k_y\sigma_y\left(k_z^2 - k_x^2\right) + k_z\sigma_z\left(k_x^2 - k_y^2\right)\right].$$

Here m^* is the effective mass of an electron, σ_0 is 2×2 unit matrix, $\boldsymbol{\sigma} = \{\sigma_x, \sigma_y, \sigma_z\}$ is a vector of Pauli spin matrices, $\mathbf{k} = \{k_x, k_y, k_z\}$ is the electron's wave vector, α characterizes the strength of the RSOI, and β is the strength of cubic spin-orbit coupling term which breaks the C_4 symmetry. It has been argued that the presence of the cubic spin-orbit coupling term in the Hamiltonian does not change transport and magnetic properties qualitatively [33]. In this work, we ignore the cubic spin-orbit coupling (H_D). As helicity operator $\mathbf{k}\cdot\boldsymbol{\sigma}/k$ commutes with the Hamiltonian H_0, from now onward we will work in the eigenbasis of the helicity operator having eigenvalues $\lambda = \pm 1$. Thus, the eigenstates of the above Hamiltonian will be $\psi_{\mathbf{k},\lambda}(\mathbf{r}) = \phi_{\mathbf{k},\lambda}e^{i\mathbf{k}\cdot\mathbf{r}}/\sqrt{\mathcal{V}}$, where $\mathcal{V}$ is volume of the system, $\lambda = \pm 1$ represents two opposite helicities, and $\phi_{\mathbf{k},\lambda}$ is helicity eigenstate which takes the following forms:

$$\phi_{\mathbf{k},+} = \begin{bmatrix}\cos(\theta/2)\\ e^{i\phi}\sin(\theta/2)\end{bmatrix}, \quad \phi_{\mathbf{k},-} = \begin{bmatrix}\sin(\theta/2)\\ -e^{i\phi}\cos(\theta/2)\end{bmatrix}. \tag{2}$$

Here, θ and ϕ are the polar and azimuthal angles, respectively, which represent the orientation of $\mathbf{k}$. The energy dispersion consists of two spin-split bands corresponding to $\lambda = \pm$ having the structure $\xi_{\mathbf{k},\lambda} = \hbar^2k^2/(2m^*) + \lambda\alpha k$. Due to distinct spin-momentum locking, these systems have different Fermi surface topologies for energy $\xi > 0$ (convex-convex shape) and $\xi < 0$ (concave-convex shape) as shown in Fig. 1. There are two Fermi wave vectors $k_\lambda^F = -\lambda k_\alpha + \sqrt{k_\alpha^2 + 2m^*\xi_F/\hbar^2}$ with $k_\alpha = m^*\alpha/\hbar^2$, corresponding to $\lambda = \pm$ bands for $\xi_F > 0$. The density of states for $\lambda = \pm$ bands becomes

$$D_\lambda^{>}(\xi_F) = D_0\left[\frac{\xi_F + 2\xi_\alpha}{\sqrt{\xi_F + \xi_\alpha}} - \lambda\sqrt{4\xi_\alpha}\right], \tag{3}$$

where $D_0 = \frac{1}{4\pi^2}(\frac{2m^*}{\hbar^2})^{\frac{3}{2}}$ and $\xi_\alpha = \hbar^2k_\alpha^2/2m^*$. The total density of states is given by $D^{>}(\xi_F) = 2D_0\frac{(\xi_F+2\xi_\alpha)}{\sqrt{\xi_F+\xi_\alpha}}$. For $\xi_F < 0$, the $\lambda = -$ band is characterized by the two branches with the Fermi wave vectors $k_\eta^F = k_\alpha - (-1)^{\eta-1}\sqrt{k_\alpha^2 + 2m^*\xi_F/\hbar^2}$ with $\eta = 1, 2$. The density of states within two concentric spherical shells with radii k_1 and k_2 is given by

$$D_\eta^{<}(\xi_F) = D_0\left[\frac{\xi_F + 2\xi_\alpha}{\sqrt{\xi_F + \xi_\alpha}} - (-1)^{\eta-1}\sqrt{4\xi_\alpha}\right], \tag{4}$$

with total density of states $D^{<}(\xi_F) = 2D_0\frac{(\xi_F+2\xi_\alpha)}{\sqrt{\xi_F+\xi_\alpha}}$. For $\xi < 0$, the $\lambda = -$ band has a nonmonotonic behavior and has a van Hove singularity in the density of states at $\xi = -\xi_\alpha$ with $\xi_{\min} = -\xi_\alpha$, similar to the conventional 1D electron gas.

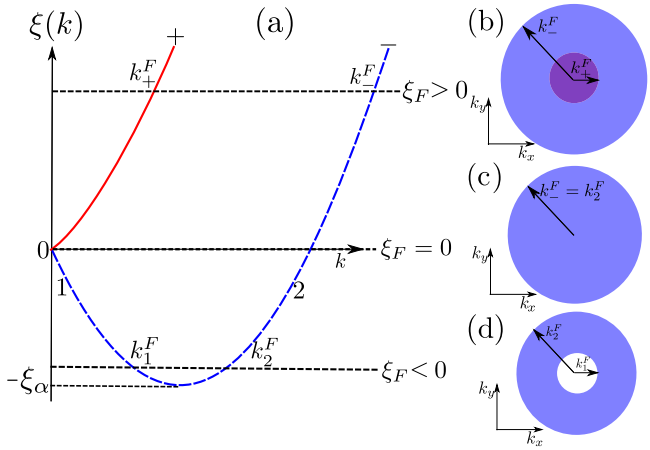

FIG. 1. (a) Energy dispersion of noncentrosymmetric metals: The $k = 0$ point where two bands touch is known as band touching point (BTP). In panels (b) and (d), the cross sections of the Fermi surfaces for $\xi_F > 0$ and $\xi_F < 0$ are shown, respectively. The Fermi surface topology is different in both cases, having convex-convex shape and concave-convex shape for $\xi_F > 0$ and $\xi_F < 0$, respectively. (c) There is only one Fermi surface at BTP ($\xi_F = 0$) where the change in the Fermi surface topology occurs.

In the $T \to 0$ limit, the Fermi energy ξ_F can be extracted from the following equation,

$$(4\xi_\alpha + \xi_F)\sqrt{\xi_\alpha + \xi_F} = \left(\xi_F^0\right)^{3/2}, \tag{5}$$

where $\xi_F^0 = \frac{\hbar^2}{2m^*}(3\pi^2 n_e)^{2/3}$ is the Fermi energy for ordinary 3D electron gas, with n_e being the density of the conduction electrons in NCMs. It can be easily seen from the above equation that $n_e = n_t$ with $n_t = 4k_\alpha^3/3\pi^2$ is the critical density of electrons where the Fermi surface topology changes which also defines the band touching point (BTP).

III. DYNAMICAL POLARIZATION FUNCTION

Within the linear response theory for translationally invariant systems, the dynamical polarization function or density-density correlation function of the two-level system in response to a time-dependent perturbation in Fourier space becomes (see Appendix A) $\chi^0_{\rho\rho}(\mathbf{q}, \omega) = \sum_{\lambda\lambda'} \chi^0_{\lambda\lambda'}(\mathbf{q}, \omega)$, with

$$\chi^0_{\lambda\lambda'}(\mathbf{q}, \omega + i0^+) = \sum_{\mathbf{k}} \frac{\mathcal{F}_{\lambda\lambda'}(\mathbf{k}, \mathbf{k}+\mathbf{q})}{\mathcal{V}} \frac{n^F_{\mathbf{k},\lambda} - n^F_{\mathbf{k}+\mathbf{q},\lambda'}}{\hbar\Omega + \xi_{\mathbf{k},\lambda} - \xi_{\mathbf{k}+\mathbf{q},\lambda'}}, \tag{6}$$

where $\hbar\Omega = \hbar(\omega + i0^+)$ and $n^F_{\mathbf{k},\lambda} = 1/[e^{\beta(\xi_{\mathbf{k},\lambda}-\mu)} + 1]$ with $\beta = (k_B T)^{-1}$, T being the temperature. Also $\mathcal{F}_{\lambda\lambda'}(\mathbf{k}, \mathbf{k}+\mathbf{q}) = |\phi^\dagger_{\mathbf{k},\lambda}\phi_{\mathbf{k}+\mathbf{q},\lambda'}|^2 = \frac{1}{2}[1 + \lambda\lambda'\frac{\mathbf{k}\cdot(\mathbf{k}+\mathbf{q})}{|\mathbf{k}||\mathbf{k}+\mathbf{q}|}]$ describes the overlap between the states labeled by $|\mathbf{k}, \lambda\rangle$ and $|\mathbf{k}+\mathbf{q}, \lambda'\rangle$. In the above notation of dynamical polarization function, the subscript $\rho\rho$ indicates that it is a density-density correlation function. Utilizing the isotropic nature of the band structure, we choose $\mathbf{q} = q\hat{z}$ for simplicity. With $x = k/k_\alpha$, $x^F_\lambda = k^F_\lambda/k_\alpha$, $Q = q/k_\alpha$, and $D_\alpha = m^* k_\alpha/(4\pi^2\hbar^2)$, performing the $\theta_{\mathbf{k}}$ integration exactly, the Lindhard function takes following form for $\xi_F > 0$ (for $T \to 0$):

$$\chi^0_{\rho\rho}(\mathbf{q}, \Omega) = D_\alpha \sum_{\lambda s} \int_0^{x^F_\lambda} \frac{dx}{Q}\left[C^s_\lambda \ln\left(\frac{t^s_{\lambda+} - 2Qx}{t^s_{\lambda+} + 2Qx}\right) + G^s_\lambda \ln\left(\frac{t^s_{\lambda-} - 2Qx}{t^s_{\lambda-} + 2Qx}\right)\right], \tag{7}$$

with $s = \pm 1$, $\zeta^s_\lambda = s\hbar\Omega/\xi_\alpha + 2\lambda x - Q^2$, $t^s_{\lambda\pm} = s(\zeta^s_\lambda + 2) \pm 2\sqrt{(x+\lambda)^2 + s\hbar\Omega/\xi_\alpha}$, $a^s_\lambda = x(\zeta^{s_\omega}_\lambda + 2\lambda x)$, $b^s_\lambda = s(\lambda - x)$, $C^s_\lambda = (a^s_\lambda + b^s_\lambda t^s_{\lambda+})/(t^s_{\lambda+} - t^s_{\lambda-})$, and $G^s_\lambda = -(a^s_\lambda + b^s_\lambda t^s_{\lambda-})/(t^s_{\lambda+} - t^s_{\lambda-})$. Now it is easy to evaluate this 1D integration numerically with the cost of $s = \pm 1$ summation. After a similar calculation, the Lindhard function for $\xi_F < 0$ (for $T \to 0$) is

$$\chi^0_{\rho\rho}(\mathbf{q}, \Omega) = D_\alpha \sum_{s} \int_{x^F_1}^{x^F_2} \frac{dx}{Q}\left[C^s_- \ln\left(\frac{t^s_{-+} - 2Qx}{t^s_{-+} + 2Qx}\right) + G^s_- \ln\left(\frac{t^s_{--} - 2Qx}{t^s_{--} + 2Qx}\right)\right], \tag{8}$$

with $s = \pm 1$ and $x^F_1 = k^F_1/k_\alpha$, $x^F_2 = k^F_2/k_\alpha$. Here k^F_η with $\eta = 1, 2$ is Fermi wave vector for the η branch of the $\lambda = -$ band for $\xi_F < 0$. While deriving the above equation, we have used the fact that $n^F_{\mathbf{k},\lambda} = 0$ for all $\mathbf{k}$ above the BTP. We use Eqs. (7) and (8) to present all our numerical results.

Nonzero $\mathrm{Im}\chi^0_{\rho\rho}(\mathbf{q}, \omega)$ for a given $(\mathbf{q}, \omega)$ describes the excitation (with excitation energy $\hbar\omega$) of an electron from an occupied state $\mathbf{k}$ below the Fermi energy to an unoccupied state $\mathbf{k}+\mathbf{q}$ above the Fermi energy and thus leaving a hole (empty state) below the Fermi level. The collection of all such points in the $(\mathbf{q}, \omega)$ plane is known as the particle-hole continuum (PHC). In other words, the system can absorb incoming energy by exciting electron-hole pairs in the region where $\mathrm{Im}\chi^0_{\rho\rho}(\mathbf{q}, \omega) \neq 0$. Outside the PHC, the system cannot absorb energy by this mechanism. For NCMs, intra- and interband PHC are shown in Fig. 2. The full PHC of NCMs below and above the BTP are of similar nature. The intraband PHC is similar to that of noninteracting 3D electron gas. It is worth mentioning here that in NCMs, for $q \to 0$, there is a finite-energy gap in between intra- and interband PHC similar to 2D systems with spin-orbit coupling, but it is in contrast to BiTeX semiconductor compounds where the interband PHC starts at zero energy. For $\xi_F > 0$ (<0), the minimum and maximum energy for electron-hole pair excitation with $q \to 0$ is $\hbar\omega = 2\alpha k^F_+$ ($2\alpha k^F_1$) and $\hbar\omega = 2\alpha k^F_-$ ($2\alpha k^F_2$), respectively. The width of interband PHC for $q \to 0$ is $\Delta^> = 8\xi_\alpha$ for $\xi_F > 0$ and $\Delta^< = 8\sqrt{\xi^2_\alpha + \xi_\alpha\xi_F}$ for $\xi_F < 0$. Due to different Fermi surface topology of NCMs for $\xi_F > 0$ and $\xi_F < 0$, $\Delta^>$ and $\Delta^<$ show different behaviors with respect to the change in the carrier density. Note that $\Delta^>$ depends only on the Rashba energy ξ_α, but $\Delta^<$ depends on both the carrier density and the Rashba energy [55]. This different behavior of width of interband PHC acts as a probe to observe the distinct Fermi surface topology of NCMs for Fermi energies below and above the BTP.

Figure 3 shows the variation of $\mathrm{Re}\chi^0_{\rho\rho}(\mathrm{q}, 0)$ with respect to the wave vector q. Note that $\mathrm{Re}\chi^0_{\rho\rho}(\mathrm{q}, 0)$ is of different nature than that of conventional 3DEG for small q but has

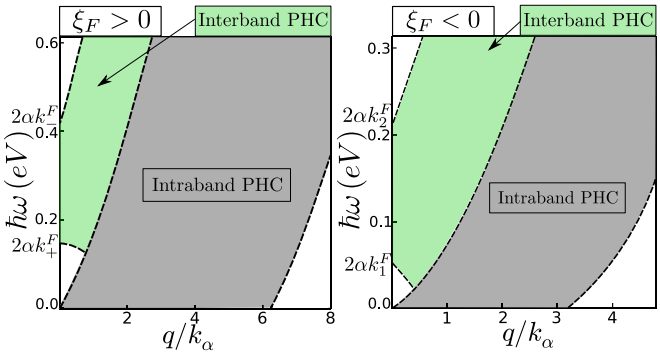

FIG. 2. Intraband and interband PHC for $\xi_F > 0$ (left) and $\xi_F < 0$ (right). Minimum and maximum excitation energies for interband transitions with $q = 0$ are $2\alpha k_+^F$ ($2\alpha k_1^F$) and $2\alpha k_-^F$ ($2\alpha k_2^F$) for $\xi_F > 0$ (<0), respectively. For $\xi_F > 0$ ($\xi_F < 0$), zero-energy intraband transitions ends at $q = 2k_-^F$ ($q = 2k_2^F$). It is interesting to note that for all carrier densities (n_e) intraband PHC of NCMs is always bigger than that of conventional 3DEG, because $2k_F^0 < 2k_-^F$ ($2k_F^0 < 2k_2^F$) for $\xi_F > 0$ (<0) with $k_F^0 = (3\pi^2 n_e)^{2/3}$ being the Fermi wave vector of conventional 3DEG. Parameters: $m^* = 0.5m_0$ with m_0 being the bare electron mass, $\alpha = 1$ eVÅ. For the left panel $n_e = 16n_\alpha$ and for the right panel $n_e = 2n_\alpha$ with $n_\alpha = k_\alpha^3/(3\pi^2)$.

similar nature for large q. Interestingly, the static Lindhard function of NCMs has distinct second and third derivative singularities owing to the nature of distinct Fermi surface topology for $\xi_F > 0$ and $\xi_F < 0$. The singularities in the static Lindhard function arise because of the fact that there is a large mismatch of number of states contributing significantly to it below and above the singular point. At the singular point, the static Lindhard function changes sharply. Another way of identifying these singular points is to look for those q for which the original Fermi surface $\xi_{\mathbf{k},\lambda}$ and the shifted Fermi

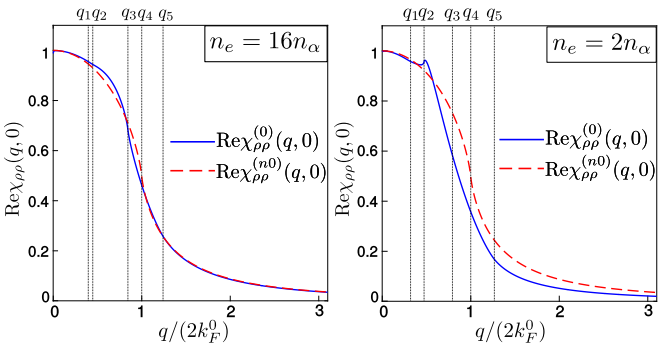

FIG. 3. Absolute static Lindhard function for NCMs $\mathrm{Re}\chi_{\rho\rho}^0(\mathrm{q},0)$ and for conventional 3DEG [17] $\mathrm{Re}\chi_{\rho\rho}^{\mathrm{n0}}(\mathrm{q},0)$ (in units of total density of states of respective systems) vs q for $n_e = 16n_\alpha$ (left panel) and $n_e = 2n_\alpha$ (right panel). $\mathrm{Re}\chi_{\rho\rho}^0(\mathrm{q},0)$ is obtained by doing the 1D numerical integration of Eqs. (7) and (8) for $\xi_F > 0$ and $\xi_F < 0$, respectively. At $n_e = 2n_\alpha$, $\xi_F < 0$ for NCMs. In this figure, q_i's (in units of $2k_F^0$) denote the wave vectors where the Lindhard function or its derivative is singular. In the left panel, these are given as $q_1 = k_-^F - k_+^F$, $q_2 = 2k_+^F$, $q_3 = k_-^F + k_+^F$, $q_4 = 2k_F^0$, and $q_5 = 2k_-^F$ in units of $2k_F^0$. In the right panel, the singular points are $q_1 = 2k_1^F$, $q_2 = k_2^F - k_1^F$, $q_3 = k_2^F + k_1^F$, $q_4 = 2k_F^0$, and $q_5 = 2k_2^F$ in units of $2k_F^0$. Parameters are $m^* = 0.5m_0$, $\alpha = 1$ eV Å.

surface $\xi_{\mathbf{k}+\mathbf{q},\lambda'}$ touch each other. We also show the singular points q_i (in units of $2k_F^0$) in Fig. 3. For $\xi_F > 0$, the static susceptibility has second derivative singularity at $q_3 = k_-^F + k_+^F = 2\sqrt{k_\alpha^2 + 2m^*\xi_F/\hbar^2} > (k_-^F - k_+^F)$ due to interband transitions similar to the conventional 3DEG and third derivative singularity at $q_2 = 2k_+^F$, $q_5 = 2k_-^F$ arising from the intraband transitions. The third derivative singularity at $q_1 = k_-^F - k_+^F = 2k_\alpha$ is weak. For $\xi_F < 0$, the second derivative singularity arises at $q_2 = k_2^F - k_1^F = 2\sqrt{k_\alpha^2 + 2m^*\xi_F/\hbar^2} < (k_2^F + k_1^F)$ due to interbranch transitions and third derivative singularities arise at $q_1 = 2k_1^F$, $q_5 = 2k_2^F$. Also, the third derivative singularity at $q_3 = k_2^F + k_1^F = 2k_\alpha$ is weak. Note that the second derivative singularity in the static Lindhard function happens at the addition (difference) of Fermi wave vectors of two bands (branches) for $\xi_F > 0 (< 0)$ as a consequence of change in the Fermi surface topology at the BTP, although the functional dependence of this singular point on α and ξ_F is the same for $\xi_F > 0$ and $\xi_F < 0$. The similar nature of singularities in the static Lindhard function was also reported in bilayer honeycomb lattice with ultracold atoms [57].

IV. PLASMONS

Using the equation of motion technique within RPA, the final expression of the Lindhard function in the presence of the electron-electron interaction $\chi_{\rho\rho}^i(\mathbf{q},\Omega)$ is given as [see Appendix C]

$$\chi_{\rho\rho}^i(\mathbf{q},\Omega) = \sum_{\lambda\lambda'} \chi_{\lambda\lambda'}^i(\mathbf{q},\Omega) = \frac{\chi_{\rho\rho}^0(\mathbf{q},\Omega)}{1 - V(\mathbf{q})\chi_{\rho\rho}^0(\mathbf{q},\Omega)}. \quad (9)$$

Here $\chi_{\rho\rho}^0(\mathbf{q},\omega)$ is the dynamical polarization function in the absence of electron-electron interaction, which is described in the previous section. The plasmons are described by the poles of the above response function, i.e., zeros of the dielectric function,

$$\epsilon(\mathbf{q},\Omega) = 1 - V(\mathbf{q})\chi_{\rho\rho}^0(\mathbf{q},\Omega), \quad (10)$$

with Fourier transform of the Coulomb potential $V(\mathbf{q}) = e^2/(\epsilon_\infty q^2)$, where $\epsilon_\infty = 20\epsilon_0$ with ϵ_∞ being the background dielectric constant and ϵ_0 is the permittivity of the vacuum. We solve $\epsilon(\mathbf{q},\Omega) = 0$ numerically using Eqs. (7) and (8) for $\xi_F > 0$ and $\xi_F < 0$, respectively. We first look for plasmon modes for Fermi energy well below and above the BTP. In this case, we get two solutions of $\epsilon(\mathbf{q},\Omega) = 0$ for a given q. Out of these two, the higher energy solution lies in between the intra- and interband PHC, where both $\mathrm{Re}[\epsilon(q,\omega)] = 0$ and $\mathrm{Im}[\epsilon(q,\omega)] = 0$, which describes the undamped optical plasmon mode. Inside intra- or interband PHC, $\mathrm{Im}\chi_{\rho\rho}^0(\mathbf{q},\omega) \neq 0$, which is responsible for the dissipation in the system. Before reaching the PHC, this plasmon mode with zero dissipation is an oscillatory eigenmode of the system with infinite life time. Inside the PHC, this plasmon mode is not an exact eigenmode of the system and acquires a finite lifetime $\propto \mathrm{Im}\chi_{\rho\rho}^0(\mathbf{q},\omega)$. So, in this region, it becomes damped; i.e., it decays to particle-hole excitations, also known as Landau damping. The other solution falls inside the PHC where $\mathrm{Im}[\epsilon(q,\omega)] \neq 0$, and therefore it is not a solution of $\epsilon(\mathbf{q},\omega) = 0$. The plasmon dispersion together with the PHC for a Fermi energy above

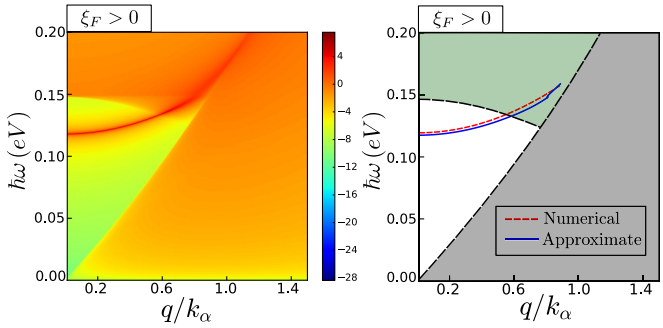

FIG. 4. Left panel: Density plot of natural logarithm of loss function defined by Eq. (11) for $\xi_F > 0$. Sharp bright line shows the undamped plasmon mode outside the PHC. Right panel: Plasmon dispersion together with PHC for $\xi_F > 0$. The solid curve shows the plasmon dispersion obtained with the use of Eq. (10) with exact dynamical polarization function calculated numerically. The dashed curve (apart from the PHC edges) shows the approximate plasmon dispersion given in Eq. (17). Parameters: $m^* = 0.5m_0$, $\alpha = 1$ eV Å, $\epsilon_\infty = 20\epsilon_0$, $n_e = 16n_\alpha$.

and below the BTP is shown in the right panels (solid curve) of Figs. 4 and 5, respectively. Here we note that there is only a single undamped optical plasmon mode in NCMs for a range of parameters.

Now it would be interesting to compare our results with that of in BiTeX semiconductor compounds [45]. There are two plasmon modes owing to their anisotropic band structure nature in BiTeX semiconductor compounds [45]. One out-of-plane plasmon mode is independent of the in-plane spin-orbit coupling (SOC). The other in-plane plasmon mode is dependent on the in-plane SOC but lies within the Rasbha continuum and hence it is Landau damped. In these bipolar semiconductor systems, the Rashba continuum is present for all energies in contrast to 2D Rashba systems [22,24], where it starts at finite energy at $q = 0$. So, the plasmon mode lies within the Rashba continuum for realistic material parameters

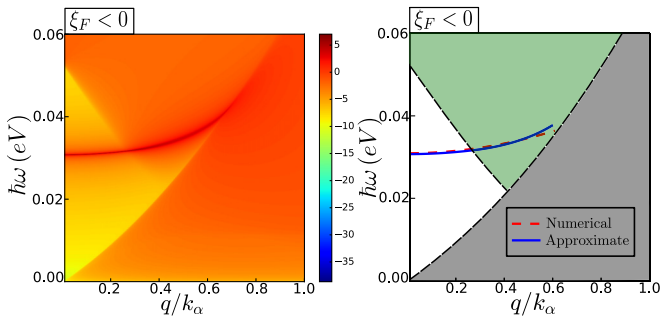

FIG. 5. Left panel: Density plot of natural logarithm of loss function defined by Eq. (11) for $\xi_F < 0$. Sharp bright line shows the undamped plasmon mode outside the PHC. Right panel: Plasmon dispersion together with PHC for $\xi_F < 0$. The solid curve shows the plasmon dispersion obtained with the use of Eq. (10) with exact dynamical polarization function calculated numerically. The dashed curve (apart from the PHC edges) shows the approximate plasmon dispersion given in Eq. (17). Parameters: $m^* = 0.5m_0$, $\alpha = 1$ eV Å, $\epsilon_\infty = 20\epsilon_0$, $n_e = 2n_\alpha$.

of these systems and hence decays into particle-hole excitations.

Plasmon modes can be directly observed in the electron-energy loss and Raman scattering experiments by measuring the dynamical structure factor. The dynamical structure factor is proportional to the loss function $-\mathrm{Im}[1/\epsilon(q,\omega)]$. In the left panels of Figs. 4 and 5, we show the density plot of the loss function for the Fermi energy well above and below the BTP in the (q, ω) plane. The loss function can be expressed as

$$-\mathrm{Im}\left[\frac{1}{\epsilon(q,\omega)}\right] = \frac{V(q)\mathrm{Im}\left[\chi^0_{\rho\rho}\right]}{\left(1 - V(q)\mathrm{Re}\left[\chi^0_{\rho\rho}\right]\right)^2 + \left(V(q)\mathrm{Im}\left[\chi^0_{\rho\rho}\right]\right)^2}. \tag{11}$$

From the above expression, it is evident that the loss function is a δ function for the plasmon mode with width of the δ function $\propto \mathrm{Im}[\chi^0_{\rho\rho}]$. Outside the PHC, for the undamped plasmon mode loss function shows a well-defined δ peak (with very small width due to finite η), which is indicated by a sharp bright line in the left panels of Figs. 4 and 5. As we go inside PHC, the width of this δ function increases and plasmon mode becomes damped. Also deep inside the PHC, the plasmon mode is overdamped and the peak in the loss function disappears, which is clearly shown in the left panels of Figs. 4 and 5. We note from Figs. 4 and 5 that the plasmon dispersion for $\xi_F < 0$ is more flat than that of $\xi_F > 0$, so the plasmon mode has smaller velocity for the Fermi energies below the BTP.

In Fig. 6, for fixed background dielectric constant, the density plot of the loss function in the $(\hbar\omega, n_e/n_\alpha)$ plane is shown for small q. A sharp bright line shows the behavior of plasma frequency ω_p (defined as the first term in the plasmon dispersion in units of $\hbar$) with respect to the carrier density n_e/n_α of the system and the lighter region compared to the sharp bright line indicates the interband PHC for small q. For a fixed α at carrier density, $n_e = n_t$ ($\xi_F = 0$) represents the BTP. It is interesting to find that as we tune the Fermi energy around the BTP, the plasmon mode becomes damped within a range of electron-electron interaction strengths. Also, with a fixed electron-electron interaction strength when Fermi energy is well below and above the BTP, the plasmon mode is undamped, but near the BTP it falls in the interband PHC and becomes damped. The reason behind this feature is that the starting point of the Rasbha continuum $2\alpha k^F_+$ ($2\alpha k^F_1$) for $\xi_F > 0$ (<0) shifts toward $\hbar\omega = 0$ as we approach the BTP from above and below. As a consequence of this, the zero of Eq. (10) starts to fall within the Rashba continuum.

Here we provide another known way [45] of observing plasmon modes through optical conductivity. It is well known that the finite value of the real part of the longitudinal conductivity $\mathrm{Re}\sigma(\mathbf{q},\omega)$, also known as optical conductivity, is responsible for the dissipation of energy in the system by Joule heating, when a current $\mathbf{J}(\mathbf{q},\omega)$ is flowing in the system. The relation between $\mathrm{Im}\chi^0_{\rho\rho}(\mathbf{q},\omega)$ and $\mathrm{Re}\sigma(\mathbf{q},\omega)$ is $\mathrm{Re}\sigma^{(0)}(\mathbf{q},\omega) = -\omega e^2 \mathrm{Im}\chi^0_{\rho\rho}(\mathbf{q},\omega)/q^2$. So, the nonvanishing $\mathrm{Im}\chi^0_{\rho\rho}(\mathbf{q},\omega)$ is also related to the dissipation of the energy in the system. From this relation, we extract the behavior of the real part of optical conductivity $\mathrm{Re}\sigma^{(0)}(\mathbf{q},\omega)$ in the absence of electron-electron interaction, which is shown in

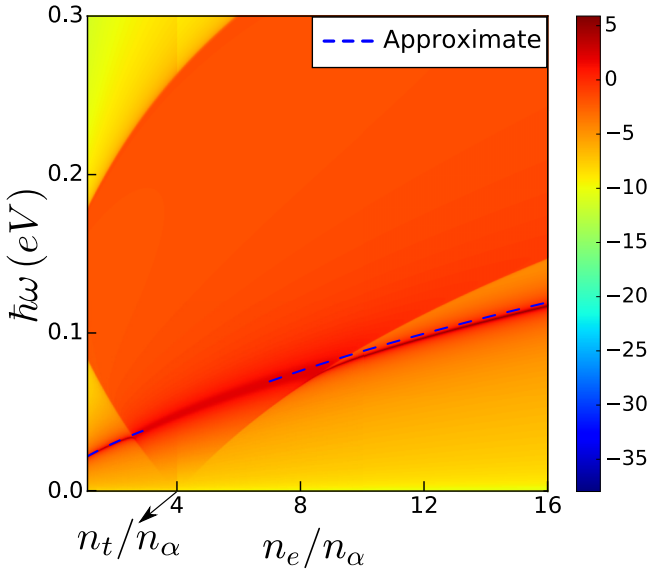

FIG. 6. Density plot of natural logarithm of loss function obtained numerically as a function of carrier density n_e (in units of n_α) and $\hbar\omega$ for small q. At carrier density $n_e = n_t$, $\xi_F = 0$ which represents the BTP. The sharp bright line outside the interband PHC indicates that the plasmon mode is undamped only when the Fermi energy ξ_F lies well below and above the BTP. Dashed curve shows the approximate plasma frequency obtained from $\omega_p^{(>/<)} \approx \omega_p'/\sqrt{\beta^{(>/<)}}$ (derived in the main text) which matches well with the sharp bright line representing the plasma frequency calculated with the help of exact numerical Lindhard function. Parameters: $m^* = 0.5m_0$, $\alpha = 1$ eV Å, $\epsilon_\infty = 20\epsilon_0$, and carrier density varies from $n_e = 1.1n_\alpha$ to $n_e = 16.0n_\alpha$.

Fig. 7 [55]. In the presence of electron-electron interaction, optical conductivity becomes (see Appendix D) $\mathrm{Re}\sigma^i(\mathbf{q},\omega) = -\omega e^2 \mathrm{Im}\chi^i_{\rho\rho}(\mathbf{q},\omega)/q^2$. Here $\mathrm{Im}\chi^i_{\rho\rho}(\mathbf{q},\omega)$ is the dynamical polarization function given in Eq. (9). In Fig. 7, for Fermi energy above (left panel) and below (right panel) the BTP,

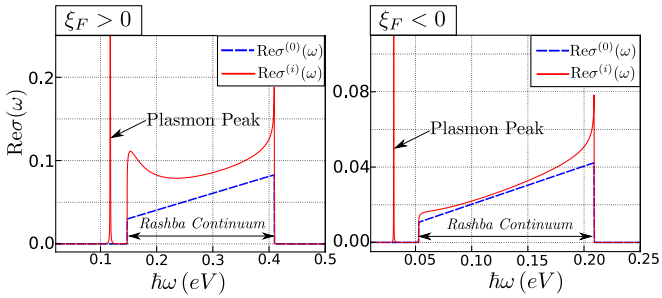

FIG. 7. Real part of optical conductivity for $\xi_F > 0$ (left panel) and $\xi_F < 0$ (right panel). Solid curve shows the behavior of the real part of optical conductivity in the presence of electron-electron interaction obtained within the RPA. The peak outside the Rasbha continuum indicates the undamped plasmon mode for $q = 0.01k_\alpha$. For completeness, we also show the behavior of the real part of optical conductivity for the noninteracting case (dashed curve) [55]. Parameters: Carrier density $n_e = 16n_\alpha$ (same as Fig. 4) for left panel and $n_e = 2n_\alpha$ (same as Fig. 5) for left panel, $\epsilon_\infty = 20\epsilon_0$ (same as Fig. 4 and Fig. 5). All other parameters are the same as Fig. 2.

we have shown the $\mathrm{Re}\sigma^{(0)}(\mathbf{q},\omega)$ and $\mathrm{Re}\sigma^{(i)}(\mathbf{q},\omega)$ by dashed and solid lines for small q, respectively. The plasmon mode shows up with a peak in $\mathrm{Re}\sigma^i(\mathbf{q},\omega)$ between intraband PHC and Rashba continuum as shown in Fig. 7. So, from the small q optical conductivity measurement in addition to the measurement of plasma frequency, one can also extract the strength of RSOI (α) by measuring the width of the Rashba continuum (same as optical width), which depends differently on carrier density and α for Fermi energies above and below the BTP.

In order to get more insight in the above observations, we derive approximate analytical expressions of the plasma frequency ω_p and plasmon dispersion. For $q \ll k_\lambda^F$, the full expression of $\chi^0_{\rho\rho}(\mathbf{q},\omega)$ is given in Appendix B. In order to find the plasma frequency ω_p, we approximate $\chi^0_{\rho\rho}(\mathbf{q},\omega)$ for $\xi_F > 0$ only up to the $O(q^2)$ term, which is given by

$$\chi^0_{\rho\rho}(\mathbf{q},\Omega) \approx \frac{8D_\alpha Q^2 \xi_\alpha^2[(x_+^F)^2 + (x_-^F)^2]\sqrt{1+\xi_F/\xi_\alpha}}{3(\hbar\Omega)^2} + \frac{Q^2 D_\alpha}{6}\ln\left[\frac{(\hbar\Omega)^2 - (4\xi_\alpha x_+^F)^2}{(\hbar\Omega)^2 - (4\xi_\alpha x_-^F)^2}\right]. \quad (12)$$

Here all the notations are the same as in the previous section with $x_\lambda^F = k_\lambda^F/k_\alpha$. For Eq. (10), the plasma frequency ω_p will be given by the zeros of the following equation,

$$1 - \left\{\frac{(\hbar\omega_p')^2}{(\hbar\Omega)^2} + \frac{D_\alpha}{6}\ln\left[\frac{(\hbar\Omega)^2 - (4\xi_\alpha x_+^F)^2}{(\hbar\Omega)^2 - (4\xi_\alpha x_-^F)^2}\right]\right\} = 0, \quad (13)$$

with

$$\omega_p' = \frac{\omega_p^n}{\sqrt{\epsilon_\infty/\epsilon_0}}\sqrt{\frac{2\xi_\alpha + \xi_F}{4\xi_\alpha + \xi_F}}, \quad (14)$$

and $\omega_p^n = \sqrt{n_e e^2/m^*\epsilon_0}$ being the plasma frequency for an ordinary 3D electron gas [17]. The above expression of ω_p' has been derived using Eq. (5). We first consider the limiting case when $\alpha = 0$. In this case, the second term in the parentheses of Eq. (13) vanishes, and by putting $\xi_\alpha = 0$ in Eq. (14), the plasma frequency $\omega_p = \omega_p^n$ reproduces the known plasma frequency for an ordinary 3D electron gas. In order to achieve an approximate expression of ω_p for nonzero α, we solve Eq. (13) for $\hbar\omega/4\xi_\alpha < 1$. The plasma frequency becomes $\omega_p \approx \omega_p'/\sqrt{\beta^>}$, with

$$\beta^> = 1 - \frac{e^2}{12\pi^2\alpha\epsilon_\infty}\ln\left[\frac{\sqrt{\xi_\alpha+\xi_F} - \sqrt{\xi_\alpha}}{\sqrt{\xi_\alpha+\xi_F} + \sqrt{\xi_\alpha}}\right]. \quad (15)$$

We have also obtained a similar approximate expression of plasma frequency for Fermi energies below the BTP. The plasmon frequency above ($>$) and below ($<$) the BTP is $\omega_p^{(>/<)} \approx \omega_p'/\sqrt{\beta^{(>/<)}}$, with

$$\beta^{(>/<)} = 1 - \frac{e^2}{12\pi^2\alpha\epsilon_\infty}\ln\left[\frac{\pm(\sqrt{\xi_\alpha+\xi_F} - \sqrt{\xi_\alpha})}{\sqrt{\xi_\alpha+\xi_F} + \sqrt{\xi_\alpha}}\right]. \quad (16)$$

The variation of plasma frequency ω_p with the Fermi energy for fixed background dielectric constant (ϵ_∞) is shown in Fig. 6. The sharp bright line describes numerically obtained ω_p and on top of that dashed lines describe the analytical result obtained from $\omega_p^{(>/<)} \approx \omega_p'/\sqrt{\beta^{(>/<)}}$.

We also find an approximate analytical expression of plasmon dispersion with the help of the approximate plasma frequency $\omega_p^{(>/<)}$ and $\chi^0_{\rho\rho}(\mathbf{q},\omega)$ in the long wavelength limit. The plasmon dispersion in the long wavelength limit above and below BTP becomes

$$\omega^{(>/<)}(q) \approx \omega_p^{(>/<)} + \frac{3}{5}\frac{(\xi_\alpha+\xi_F)}{m^*\omega_p^{(>/<)}}q^2$$

$$\approx \omega_p^{(>/<)} + \frac{3}{10}\frac{(v^F_{>/<}q)^2}{\omega_p^{(>/<)}}, \tag{17}$$

with $v^F_>$ ($v^F_<$) being the absolute value of the Fermi velocity for $\xi_F > 0$ (<0), which can be expressed as $v^F_> = \hbar(k^F_\lambda + \lambda)/m^* = (\hbar k_\alpha/m^*)\sqrt{1+\xi_F/\xi_\alpha}$ and $v^F_< = \hbar|(k^F_\eta - 1)|/m^* = (\hbar k_\alpha/m^*)\sqrt{1+\xi_F/\xi_\alpha}$. The absolute value of Fermi velocity increases with increase of carrier density or equivalently the Fermi energy. This implies that the plasmon mode for Fermi energy below the BTP has smaller velocity ($\propto\sqrt{\xi_F+\xi_\alpha}$) than the plasmon mode for Fermi energy above the BTP, as mentioned earlier from numerical results (see right panels of Figs. 4 and 5). Also, for all carrier densities, the stronger spin-orbit coupling reduces the Fermi energy and Fermi velocity ($\propto\sqrt{\xi_F+\xi_\alpha}$) of the system, so the plasmon velocity ($\propto\sqrt{\xi_F+\xi_\alpha}$) also decreases. The above equation also indicates that in the long wavelength limit the plasmon dispersion is $\propto q^2$, which is similar to that of an ordinary 3D electron gas [17]. This approximate plasmon dispersion has been shown in the right panels of Figs. 4 and 5 together with the exact plasmon dispersion obtained numerically. It is evident from the right panels of Figs. 4, 5, and 6 that the approximate plasma frequency and plasmon dispersion match well with the exact numerical dispersion in the long wavelength limit when the excitation energy for the plasmon is smaller than $4\xi_\alpha$. For higher or comparable excitation energy, which happens at larger carrier densities, the approximate plasmon dispersion starts to deviate from the exact numerical dispersion. Also, as we have already discussed, in the limiting case, i.e., $\alpha = 0$, $\omega_p = \omega_p^n$. Applying this to above equation for plasmon dispersion reproduces the correct form of the plasmon dispersion in the long-wavelength limit for an ordinary 3D electron gas [17].

For all the results in Figs. 4 to 7 shown above, we have taken the background dielectric constant [45,58] $\epsilon_\infty = 20\epsilon_0$. We also show in Figs. 8 and 9 that for fixed carrier densities above and below the BTP, changing the strength of electron-electron interaction which is inversely proportional to the background dielectric constant ϵ_∞ for the Fermi energy above and below the BTP does not change the number of undamped plasmon modes, although the damped plasmon modes in the interband PHC are more in number. It is also clear from Figs. 8 and 9 that for small ϵ_∞ the plasma frequency decreases rapidly and after that decreases slowly with further increase in ϵ_∞. As the Fermi energy is fixed, the interband PHC is also fixed and only the zeros of $\epsilon(\mathbf{q},\omega) = 0$ are changing with ϵ_∞. In the left panels of Figs. 8 and 9, the dashed line shows the variation of approximate plasma frequency ω_p with respect to ϵ_∞. The approximate plasma frequency matches well with its numerical counterpart for a larger background dielectric constant.

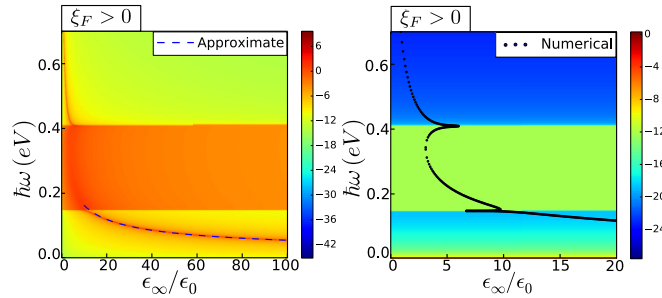

FIG. 8. Left panel: Density plot of the natural logarithm of loss function in the (ϵ_∞, ω) plane for $\xi_F > 0$ in the long wavelength limit. Dashed curve shows the variation of approximate plasma frequency ω_p as a function of ϵ_∞ which determines the interaction strength $\propto 1/\epsilon_\infty$. Right panel: Density plot of the natural logarithm of the imaginary part of the Lindhard function in (ϵ_∞, ω) plane for $\xi_F > 0$ in the long wavelength limit. Dotted curve shows the plasma frequency as a function of ϵ_∞ obtained numerically from zeros of Eq. (10) with the help of the exact Lindhard function. Parameters: $m^* = 0.5m_0$, $\alpha = 1$ eV Å, $n_e = 16n_\alpha$, $q = 0.01k_\alpha$.

V. SUMMARY AND DISCUSSION

In summary, we have studied the dynamical polarization function and plasmon modes of NCMs in detail. In NCMs, the Rashba continuum is similar to that of 2DEG with spin-orbit coupling, and it starts at finite energy, in contrast to the BiTeX semiconductor compounds [45]. In the long wavelength limit, the width of Rashba continuum behaves differently for Fermi energies below and above the BTP as a consequence of the change in the Fermi surface topology. Within a range of electron-electron interaction strengths and suitable material parameters, there is a single undamped optical plasmon mode for Fermi energies above and below the BTP. Interestingly, we find that the plasmon mode is damped for Fermi energies near the BTP within a range of electron-electron interaction strength. For fixed carrier densities above and below

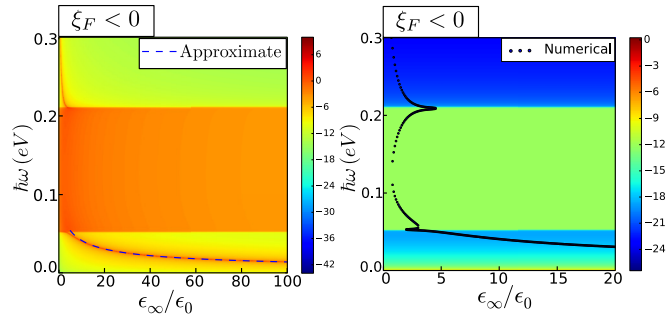

FIG. 9. Left panel: Density plot of the natural logarithm of loss function in the (ϵ_∞, ω) plane for $\xi_F < 0$ in the long wavelength limit. Dashed curve shows the variation of approximate plasma frequency ω_p as a function of ϵ_∞. Right panel: Density plot of the natural logarithm of the imaginary part of the Lindhard function in the (ϵ_∞, ω) plane for $\xi_F < 0$ in the long wavelength limit. Dotted curve shows the plasma frequency as a function of ϵ_∞ obtained numerically from zeros of Eq. (10) with the help of the exact Lindhard function. Parameters: $m^* = 0.5m_0$, $\alpha = 1$ eV Å, $n_e = 2n_\alpha$, $q = 0.01k_\alpha$.

the BTP, with the increase of background dielectric constant, the number of undamped plasmon modes does not change, although the damped plasmon modes can be more in number. It is important to note here that for a fixed electron-electron interaction strength and a range of Fermi energies or vice versa with other material parameters, NCMs always has one undamped plasmon mode. So, for the same range of realistic material parameters, NCMs host a single undamped plasmon mode whereas the plasmon modes are always damped in BiTeX semiconductor compounds [45].

In NCMs, the approximate plasma frequency and the plasmon dispersion ($\propto q^2$) matches well with the exact numerical results in the long wavelength limit. The velocity of plasmon mode is $\propto\sqrt{\xi_F+\xi_\alpha}$. So, for Fermi energies below the BTP, the plasmon mode has a smaller velocity compared to that of Fermi energies above the BTP. At fixed electron-electron interaction strength, the plasma frequency has a similar carrier density dependence for Fermi energies above and below the BTP. For Fermi energies above and below the BTP, the plasma frequency decreases rapidly for smaller ϵ_∞ and after that decreases slowly with further increase in ϵ_∞. The approximate plasma frequency as a function of ϵ_∞ also matches well with the exact numerical result for larger ϵ_∞. It is important to note that the approximate analytical expression of plasma frequency and plasmon dispersion are valid for $\hbar\omega/4\xi_\alpha < 1$ in the long wavelength limit.

It should be mentioned here that for small β the presence of cubic spin-orbit coupling term in the effective Hamiltonian may not change the dielectric properties significantly. However, for large β, it may give rise to anisotropic plasmon modes similar to the 2D electron [22] and hole gas [23]. Moreover, if the bands around other symmetry points in Brillouin zone cross the Fermi energy, they may also contribute to the dielectric properties in some form [33].

ACKNOWLEDGMENTS

We would like to thank H. A. Fertig (IU Bloomington) for some useful discussion. A.K. and S.V. acknowledge support from the SERB (Govt. of India) via sanction no. ECR/2018/001443, DAE (Govt. of India) via sanction no. 58/20/15/2019-BRNS, as well as MHRD (Govt. of India) via sanction no. SPARC/2018-2019/P538/SL. We also acknowledge HPC facility of IIT Kanpur for computational work.

APPENDIX A: THE SECOND QUANTIZED REPRESENTATION

In order to study many-body systems, it is convenient to work in the occupation number or second quantized representation [17,18]. For translationally invariant systems, we choose a single-particle basis $\{|\mathbf{k}\sigma\rangle\}$ with $\sigma=\uparrow,\downarrow$ and $\langle\mathbf{r}|\mathbf{k}\sigma\rangle=\tilde{\psi}_{\mathbf{k},\sigma}(\mathbf{r})=\eta_\sigma e^{i\mathbf{k}\cdot\mathbf{r}}/\sqrt{\mathcal{V}}$ with $\eta_\uparrow=\{10\}^\mathcal{T}$ and $\eta_\downarrow=\{01\}^\mathcal{T}$, where $\mathcal{T}$ stands for transpose. As particles are indistinguishable, the basis states in the occupation number representation is $\{|n_{\mathbf{k}\sigma}\rangle\}$ such that $\sum_{\mathbf{k}\sigma}n_{\mathbf{k}\sigma}=N$, where N is the total number of particles. We define electron creation $\tilde{C}^\dagger_{\mathbf{k},\sigma}$ and annihilation operator $\tilde{C}_{\mathbf{k},\sigma}$ with spin σ, which increases and decreases the occupation number of state $|n_{\mathbf{k}\sigma}\rangle$ by unity, respectively. All first quantized operators can be expressed in the second quantized form using the quantum field operators defined as

$$\tilde{\Psi}^\dagger(\mathbf{r})=\sum_{\mathbf{k},\sigma}\frac{e^{-i\mathbf{k}\cdot\mathbf{r}}}{\sqrt{\mathcal{V}}}\eta^\dagger_\sigma\tilde{C}^\dagger_{\mathbf{k},\sigma}\quad\text{and}\quad\tilde{\Psi}(\mathbf{r})=\sum_{\mathbf{k},\sigma}\frac{e^{i\mathbf{k}\cdot\mathbf{r}}}{\sqrt{\mathcal{V}}}\eta_\sigma\tilde{C}_{\mathbf{k},\sigma}. \tag{A1}$$

Density operator in the second quantized form is given by

$$\hat{\rho}(\mathbf{r})=\int d\mathbf{r}'\tilde{\Psi}^\dagger(\mathbf{r}')\delta(\mathbf{r}-\mathbf{r}')\tilde{\Psi}(\mathbf{r}'),\quad=\tilde{\Psi}^\dagger(\mathbf{r})\tilde{\Psi}(\mathbf{r}),\quad=\frac{1}{\mathcal{V}}\sum_{\mathbf{q}}e^{i\mathbf{q}\cdot\mathbf{r}}\hat{\rho}(\mathbf{q}),\quad\text{with}\quad\hat{\rho}(\mathbf{q})=\sum_{\mathbf{k}\sigma}\tilde{C}^\dagger_{\mathbf{k},\sigma}\tilde{C}_{\mathbf{k}+\mathbf{q},\sigma}. \tag{A2}$$

The Hamiltonian is diagonal in the helicity basis $|\mathbf{k}\lambda\rangle$ with $\lambda=\pm$. We define quantum field operators in this basis as

$$\Psi^\dagger(\mathbf{r})=\sum_{\mathbf{k},\lambda}\frac{e^{-i\mathbf{k}\cdot\mathbf{r}}}{\sqrt{\mathcal{V}}}\phi^\dagger_{\mathbf{k},\lambda}C^\dagger_{\mathbf{k},\lambda}\quad\text{and}\quad\Psi(\mathbf{r})=\sum_{\mathbf{k},\lambda}\frac{e^{i\mathbf{k}\cdot\mathbf{r}}}{\sqrt{\mathcal{V}}}\phi_{\mathbf{k},\lambda}C_{\mathbf{k},\lambda}. \tag{A3}$$

Now the Hamiltonian H_0 and the density operator in the second quantized form in the helicity basis are

$$\hat{H}_0=\sum_{\mathbf{k},\lambda}\xi_{\mathbf{k},\lambda}C^\dagger_{\mathbf{k},\lambda}C_{\mathbf{k},\lambda},\quad\text{with}\quad\xi_{\mathbf{k},\lambda}=\hbar^2k^2/(2m^*)+\lambda\alpha k.\quad\hat{\rho}(\mathbf{q})=\sum_{\mathbf{k}\lambda_1\lambda_2}\phi^\dagger_{\mathbf{k},\lambda_1}\phi_{\mathbf{k}+\mathbf{q},\lambda_2}C^\dagger_{\mathbf{k},\lambda_1}C_{\mathbf{k}+\mathbf{q},\lambda_2}. \tag{A4}$$

Consider the perturbed Hamiltonian $\hat{H}(t)=\hat{H}_0+\int d\mathbf{r}V_{\text{ext}}(\mathbf{r},t)\hat{\rho}(\mathbf{r})$. The induced density due to this perturbation is given by [17,18]

$$\rho_{\text{ind}}(\mathbf{r},t)=\int_{-\infty}^{t}dt'\int d\mathbf{r}'\chi^0_{\rho\rho}(\mathbf{r},\mathbf{r}',t,t')V_{\text{ext}}(\mathbf{r}',t'). \tag{A5}$$

Here $\chi^0_{\rho\rho}(\mathbf{r},\mathbf{r}',t,t')$, which is known as the retarded density-density response function, is the response of the density operator averaged over the ground state of perturbed Hamiltonian due to the perturbation. The $\rho\rho$ in the subscript indicates that it is a density-density correlation function. The induced density is $\rho_{\text{ind}}(\mathbf{r},t)\equiv\langle\hat{\rho}(\mathbf{r},t)\rangle_{\text{ext}}-\langle\hat{\rho}(\mathbf{r},t)\rangle_0$. The symbols $\langle\ldots\rangle_{\text{ext}}$ and $\langle\ldots\rangle_0$ denote the average is taken over the ground state of the perturbed $\hat{H}(t)$ and unperturbed Hamiltonian $\hat{H}_0$. Within the linear

response formalism [17,18], the retarded density-density response function has the following form:

$$\chi^0_{\rho\rho}(\mathbf{r},\mathbf{r}',t,t') = -\frac{i}{\hbar}\theta(t-t')\langle[\hat{\rho}(\mathbf{r},t),\hat{\rho}(\mathbf{r}',t')]\rangle_0. \tag{A6}$$

For translationally invariant systems, the density-density response function in Fourier space is given by

$$\chi^0_{\rho\rho}(\mathbf{q},t,t') = -\frac{i}{\hbar\mathcal{V}}\theta(t-t')\langle[\hat{\rho}(\mathbf{q},t),\hat{\rho}(-\mathbf{q},t')]\rangle_0. \tag{A7}$$

In the above expressions, the time dependence of the operators comes in the form $\hat{A}(t) = e^{i\hat{H}_0 t/\hbar}\hat{A}(0)e^{-i\hat{H}_0 t/\hbar}$. After some straightforward algebra, the final expression of the density-density response function in Fourier space $\chi^0_{\rho\rho}(\mathbf{q},\omega) = \int_{-\infty}^{+\infty} dt e^{i\omega(t-t')}\chi^0_{\rho\rho}(\mathbf{q},t-t')$ becomes

$$\chi^0_{\rho\rho}(\mathbf{q},\omega) = \sum_{\lambda\lambda'}\chi^0_{\lambda\lambda'}(\mathbf{q},\omega), \quad \text{with} \quad \chi^0_{\lambda\lambda'}(\mathbf{q},\omega) = \frac{1}{\mathcal{V}}\sum_{\mathbf{k}}\mathcal{F}_{\lambda\lambda'}(\mathbf{k},\mathbf{k}+\mathbf{q})\frac{n^F_{\mathbf{k},\lambda} - n^F_{\mathbf{k}+\mathbf{q},\lambda'}}{\hbar(\omega+i0^+) + \xi_{\mathbf{k},\lambda} - \xi_{\mathbf{k}+\mathbf{q},\lambda'}}. \tag{A8}$$

Here $\mathcal{F}_{\lambda\lambda'}(\mathbf{k},\mathbf{k}+\mathbf{q}) = |\phi^\dagger_{\mathbf{k},\lambda}\phi_{\mathbf{k}+\mathbf{q},\lambda'}|^2$ describes the overlap between the two states labeled by $|\mathbf{k},\lambda\rangle$ and $|\mathbf{k}+\mathbf{q},\lambda'\rangle$. Also, $n^F_{\mathbf{k},\lambda} = 1/[e^{-\beta(\xi_{\mathbf{k},\lambda}-\mu)}+1]$ is the Fermi-Dirac distribution function with $\beta = (k_B T)^{-1}$ and T being the temperature.

In order to get the full $\mathbf{q}$ and ω dependence of $\chi^0_{\rho\rho}(\mathbf{q},\omega)$, first we simplify its expression for appropriate numerical simulation. We have also derived an asymptotic expression of $\chi^0_{\rho\rho}(\mathbf{q},\omega)$ for $q \ll k^F_{\lambda/\eta}$, which we will describe in a later section. Using the ground-state properties of NCS metals, we simplify $\chi^0_{\rho\rho}(\mathbf{q},\omega)$ for $\xi_F > 0$ as follows:

$$\chi^0_{\rho\rho}(\mathbf{q},\omega) = \frac{1}{2\mathcal{V}}\sum_{\mathbf{k}\lambda\lambda'}\left[1+\lambda\lambda'\frac{\mathbf{k}\cdot(\mathbf{k}+\mathbf{q})}{|\mathbf{k}||\mathbf{k}+\mathbf{q}|}\right]\frac{n^F_{\mathbf{k},\lambda} - n^F_{\mathbf{k}+\mathbf{q},\lambda'}}{\hbar\Omega + \xi_{\mathbf{k},\lambda} - \xi_{\mathbf{k}+\mathbf{q},\lambda'}}, \quad = \chi^{0(+)}_{\rho\rho}(\mathbf{q},\omega) + \chi^{0(-)}_{\rho\rho}(\mathbf{q},\omega), \tag{A9}$$

where $\chi^{0(+)}_{\rho\rho}(\mathbf{q},\omega)$ has the following expression (for $T \to 0$):

$$\begin{aligned}\chi^{0(+)}_{\rho\rho}(\mathbf{q},\omega) &= \frac{1}{2\mathcal{V}}\sum_{\mathbf{k}\lambda\lambda'}\left[1+\lambda\lambda'\frac{\mathbf{k}\cdot(\mathbf{k}+\mathbf{q})}{|\mathbf{k}||\mathbf{k}+\mathbf{q}|}\right]\frac{n^F_{\mathbf{k},\lambda}}{\hbar\Omega + \xi_{\mathbf{k},\lambda} - \xi_{\mathbf{k}+\mathbf{q},\lambda'}}, \\ &= D_\alpha\sum_\lambda\int_0^{x^F_\lambda} x^2 dx\int_0^\pi \sin\theta_{\mathbf{k}} d\theta_{\mathbf{k}}\left[\frac{2(\zeta^+_\lambda - 2Qx\cos\theta_{\mathbf{k}}) + 4\lambda(x+Q\cos\theta_{\mathbf{k}})}{(\zeta^+_\lambda - 2Qx\cos\theta_{\mathbf{k}})^2 - 4|\mathbf{x}+\mathbf{Q}|^2}\right],\end{aligned} \tag{A10}$$

with $x = k/k_\alpha$, $x^F_\lambda = k^F_\lambda/k_\alpha$, $Q = q/k_\alpha$, $D_\alpha = m^* k_\alpha/(4\pi^2\hbar^2)$, and $\zeta^+_\lambda = \hbar\Omega/\xi_\alpha + 2\lambda x - Q^2$. After doing the straightforward $\theta_{\mathbf{k}}$ integration, $\chi^{0(+)}_{\rho\rho}(\mathbf{q},\omega)$ has the following form:

$$\chi^{0(+)}_{\rho\rho}(\mathbf{q},\omega) = D_\alpha\sum_\lambda\int_0^{x^F_\lambda}\frac{dx}{Q}\left[C^+_\lambda\ln\left(\frac{t^+_{\lambda+}-2Qx}{t^+_{\lambda+}+2Qx}\right) + G^+_\lambda\ln\left(\frac{t^+_{\lambda-}-2Qx}{t^+_{\lambda-}+2Qx}\right)\right], \tag{A11}$$

with $t^+_{\lambda\pm} = (\zeta^+_\lambda+2) \pm 2\sqrt{(x+\lambda)^2 + \hbar\Omega/\xi_\alpha}$, $C^+_\lambda = (a^+_\lambda + b^+_\lambda t^+_{\lambda+})/(t^+_{\lambda+} - t^+_{\lambda-})$, $G^+_\lambda = -(a^+_\lambda + b^+_\lambda t^+_{\lambda-})/(t^+_{\lambda+} - t^+_{\lambda-})$, $a^+_\lambda = x(\zeta^+_\lambda + 2\lambda x)$, and $b^+_\lambda = \lambda - x$. The above 1D integration can be done numerically. Now let us consider $\chi^{0(-)}_{\rho\rho}(\mathbf{q},\omega)$:

$$\begin{aligned}\chi^{0(-)}_{\rho\rho}(\mathbf{q},\omega) &= \frac{1}{2\mathcal{V}}\sum_{\mathbf{k}\lambda\lambda'}\left[1+\lambda\lambda'\frac{\mathbf{k}\cdot(\mathbf{k}+\mathbf{q})}{|\mathbf{k}||\mathbf{k}+\mathbf{q}|}\right]\frac{-n^F_{\mathbf{k}+\mathbf{q},\lambda'}}{\hbar\Omega + \xi_{\mathbf{k},\lambda} - \xi_{\mathbf{k}+\mathbf{q},\lambda'}}, \\ &= \frac{1}{2\mathcal{V}}\sum_{\mathbf{k}\lambda\lambda'}\left[1+\lambda\lambda'\frac{(\mathbf{k}-\mathbf{q})\cdot\mathbf{k}}{|\mathbf{k}-\mathbf{q}||\mathbf{k}|}\right]\frac{n^F_{\mathbf{k},\lambda'}}{-\hbar\Omega + \xi_{\mathbf{k},\lambda'} - \xi_{\mathbf{k}-\mathbf{q}\lambda}}.\end{aligned} \tag{A12}$$

Doing similar manipulations as for $\chi^{0(+)}_{\rho\rho}(\mathbf{q},\omega)$, the final expression of $\chi^{0(-)}_{\rho\rho}(\mathbf{q},\omega)$ becomes

$$\chi^{0(-)}_{\rho\rho}(\mathbf{q},\omega) = D_\alpha\sum_{\lambda'}\int_0^{x^F_{\lambda'}}\frac{dx}{Q}\left[C^-_{\lambda'}\ln\left(\frac{t^-_{\lambda+}-2Qx}{t^-_{\lambda+}+2Qx}\right) + G^-_{\lambda'}\ln\left(\frac{t^-_{\lambda-}-2Qx}{t^-_{\lambda-}+2Qx}\right)\right], \tag{A13}$$

with $\zeta^-_{\lambda'} = -\hbar\Omega/\xi_\alpha + 2\lambda' x - Q^2$, $t^-_{\lambda'\pm} = -(\zeta^-_{\lambda'}+2) \pm 2\sqrt{(x+\lambda')^2 - \hbar\Omega/\xi_\alpha}$, $C^-_{\lambda'} = (a^-_{\lambda'} + b^-_{\lambda'}t^-_{\lambda'+})/(t^-_{\lambda'+} - t^-_{\lambda'-})$, $G^-_{\lambda'} = -(a^-_\lambda + b^-_{\lambda'}t^-_{\lambda'-})/(t^-_{\lambda'+} - t^-_{\lambda'-})$, $a^-_{\lambda'} = x(\zeta^-_{\lambda'} + 2\lambda' x)$, and $b^-_{\lambda'} = -(\lambda' - x)$. We combine $\chi^{0(+)}_{\rho\rho}(\mathbf{q},\omega)$ and $\chi^{0(-)}_{\rho\rho}(\mathbf{q},\omega)$ and get the following expression of the Lindhard function for $\xi_F > 0$,

$$\chi^0_{\rho\rho}(\mathbf{q},\omega) = D_\alpha\sum_{\lambda s}\int_0^{x^F_\lambda}\frac{dx}{Q}\left[C^s_\lambda\ln\left(\frac{t^s_{\lambda+}-2Qx}{t^s_{\lambda+}+2Qx}\right) + G^s_\lambda\ln\left(\frac{t^s_{\lambda-}-2Qx}{t^s_{\lambda-}+2Qx}\right)\right], \tag{A14}$$

with $s=\pm1$, $\zeta^s_\lambda = s\hbar\Omega/\xi_\alpha + 2\lambda x - Q^2$, $t^s_{\lambda\pm} = s(\zeta^s_\lambda+2) \pm 2\sqrt{(x+\lambda)^2 + s\hbar\Omega/\xi_\alpha}$, $C^s_\lambda = (a^s_\lambda + b^s_\lambda t^{s_\omega}_{\lambda+})/(t^s_{\lambda+} - t^s_{\lambda-})$, $G^s_\lambda = -(a^s_\lambda + b^s_\lambda t^s_{\lambda-})/(t^s_{\lambda+} - t^s_{\lambda-})$, $a^s_\lambda = x(\zeta^s_\lambda + 2\lambda x)$, and $b^s_\lambda = s(\lambda - x)$.

After a similar calculation, the Lindhard function for $\xi_F < 0$ (for $T \to 0$) is given by

$$\chi^0_{\rho\rho}(\mathbf{q},\omega) = D_\alpha \sum_s \int_{x_1^F}^{x_2^F} \frac{dx}{Q}\left[C^s_{\lambda'} \ln\left(\frac{t^s_{\lambda'+} - 2Qx}{t^s_{\lambda'+} + 2Qx}\right) + G^s_{\lambda'} \ln\left(\frac{t^s_{\lambda'-} - 2Qx}{t^s_{\lambda'-} + 2Qx}\right)\right], \tag{A15}$$

with $\lambda' = -1$, $s=\pm1$, $x_1^F = k_1^F/k_\alpha$, and $x_2^F = k_2^F/k_\alpha$. While deriving the above equation, we have used the fact that $n^F_{\mathbf{k},\lambda} = 0$ for all $\mathbf{k}$ above the band crossing point.

APPENDIX B: ASYMPTOTIC EXPRESSION OF $\chi^0_{\rho\rho}(\mathbf{q},\omega)$

In this section, we derive an asymptotic expression of the dynamical polarization function, which will be helpful in finding the approximate analytical forms of plasma frequency and plasmon dispersion of NCMs. Let us first consider $\xi_F > 0$. We consider $\mathbf{q} = q\hat{z}$ for simplicity due to the isotropic nature of the band structure. For small wave vector $q \ll k^F_\lambda$,

$$\xi_{\mathbf{k},\lambda} - \xi_{\mathbf{k}+\mathbf{q},\lambda'} = \xi_{\mathbf{k},\lambda} - \xi_{\mathbf{k},\lambda'} - \mathbf{q}\cdot\nabla_{\mathbf{k}}\xi_{\mathbf{k},\lambda'} \simeq \alpha k(\lambda-\lambda') - \hbar v^k_{\lambda'} k_\alpha Q\cos\theta_{\mathbf{k}}, \tag{B1}$$

and for $T \to 0$,

$$n^F_{\mathbf{k},\lambda} - n^F_{\mathbf{k}+\mathbf{q},\lambda'} = n^F_{\mathbf{k},\lambda} - n^F_{\mathbf{k},\lambda'} - \frac{\partial n^F_{\mathbf{k},\lambda'}}{\partial\xi_{\mathbf{k},\lambda'}}\mathbf{q}\cdot\nabla_{\mathbf{k}}\xi_{\mathbf{k},\lambda'} \simeq n^F_{\mathbf{k},\lambda} - n^F_{\mathbf{k},\lambda'} + \delta(\xi_{\mathbf{k},\lambda'} - \xi_F)\hbar v^k_{\lambda'} k_\alpha Q\cos\theta_{\mathbf{k}}, \tag{B2}$$

with $v^k_{\lambda'} = \hbar(k + \lambda' k_\alpha)/m^*$. So, the Lindhard function will be

$$\begin{aligned}
\chi^0_{\rho\rho}(\mathbf{q},\omega) &= \frac{1}{2\mathcal{V}}\sum_{\mathbf{k}\lambda\lambda'}\left[1 + \lambda\lambda'\frac{\mathbf{k}\cdot(\mathbf{k}+\mathbf{q})}{|\mathbf{k}||(\mathbf{k}+\mathbf{q})|}\right]\frac{n^F_{\mathbf{k},\lambda} - n^F_{\mathbf{k}+\mathbf{q},\lambda'}}{\hbar\Omega + \xi_{\mathbf{k},\lambda} - \xi_{\mathbf{k}+\mathbf{q},\lambda'}},\\
&\simeq \frac{1}{8\pi^2}\sum_{\lambda\lambda'}\int_0^\infty k^2dk\int_0^\pi \sin\theta_{\mathbf{k}}d\theta_{\mathbf{k}}\left[1 + \lambda\lambda'\Big(1+\frac{q}{k}\cos\theta_{\mathbf{k}}\Big)\Big(1 + \frac{q^2}{k^2} + 2\frac{q}{k}\cos\theta_{\mathbf{k}}\Big)^{-1/2}\right]\\
&\quad\times\frac{\left[n^F_{\mathbf{k},\lambda} - n^F_{\mathbf{k},\lambda'} + \delta(\xi_{\mathbf{k},\lambda'} - E_F)\hbar v^k_{\lambda'}k_\alpha Q\cos\theta_{\mathbf{k}}\right]}{\hbar\Omega + \alpha k(\lambda-\lambda') - \hbar v^k_{\lambda'}k_\alpha Q\cos\theta_{\mathbf{k}}}\\
&= \chi^{0(3)}_{\rho\rho}(\mathbf{q},\omega) + \chi^{0(2)}_{\rho\rho}(\mathbf{q},\omega) + \chi^{0(1)}_{\rho\rho}(\mathbf{q},\omega).
\end{aligned} \tag{B3}$$

Here $\chi^{0(1)}_{\rho\rho}(\mathbf{q},\omega) + \chi^{0(2)}_{\rho\rho}(\mathbf{q},\omega)$ is

$$\begin{aligned}
\chi^{0(2)}_{\rho\rho}(\mathbf{q},\omega) + \chi^{0(1)}_{\rho\rho}(\mathbf{q},\omega) &= \frac{1}{8\pi^2}\sum_{\lambda\lambda'}\int_0^\infty k^2dk\int_0^\pi \sin\theta_{\mathbf{k}}d\theta_{\mathbf{k}}\left[1 + \lambda\lambda'\Big(1+\frac{q}{k}\cos\theta_{\mathbf{k}}\Big)\Big(1 + \frac{q^2}{k^2} + 2\frac{q}{k}\cos\theta_{\mathbf{k}}\Big)^{-1/2}\right]\\
&\quad\times\frac{\delta(\xi_{\mathbf{k},\lambda'} - \xi_F)\hbar v^k_{\lambda'}k_\alpha Q\cos\theta_{\mathbf{k}}}{\hbar\Omega + \alpha k(\lambda-\lambda') - \hbar v^k_{\lambda'}k_\alpha Q\cos\theta_{\mathbf{k}}}\\
&= \frac{mk_\alpha}{8\pi^2\hbar^2}\sum_{\lambda\lambda'}\frac{\left(x^F_{\lambda'}\right)^2}{\left|x^F_{\lambda'} + \lambda'\right|}\int_{-1}^1 d\tau\left[1 + \lambda\lambda'\Big(1+\frac{Q\tau}{x^F_{\lambda'}}\Big)\Big(1 + \frac{Q^2}{\left(x^F_{\lambda'}\right)^2} + 2\frac{Q\tau}{x^F_{\lambda'}}\Big)^{-1/2}\right]\\
&\quad\times\gamma^{\lambda'}_\lambda\left(x^F_{\lambda'},\Omega\right)Q\tau\left(1 - \gamma^{\lambda'}_\lambda\left(x^F_{\lambda'},\Omega\right)Q\tau\right)^{-1},
\end{aligned} \tag{B4}$$

where $\tau = \cos\theta_{\mathbf{k}}$, $x^F_{\lambda'} = k^F_{\lambda'}/k_\alpha$, $Q = q/k_\alpha$, $v^x_{\lambda'} = \hbar k_\alpha(x+\lambda')/m^*$, and $\gamma^{\lambda'}_\lambda(x,\Omega) = \hbar v^x_{\lambda'}k_\alpha/\Delta^{\lambda'}_\lambda(x,\Omega)$ with $\Delta^{\lambda'}_\lambda(x,\Omega) = \hbar\Omega + \alpha k_\alpha x(\lambda-\lambda')$. It is easy to see that $\gamma^+_+(x^F_+,\Omega) \equiv \gamma^+_+ = \hbar v^{x^F_+}_+ k_\alpha/\hbar\Omega$, $\gamma^-_-(x^F_-,\Omega) \equiv \gamma^-_- = \hbar v^{x^F_-}_- k_\alpha/\hbar\Omega$, $\gamma^-_+(x^F_-,\Omega) \equiv \gamma^-_+ = \hbar v^{x^F_-}_- k_\alpha/(\hbar\Omega + 2\alpha k_\alpha x^F_-)$, and $\gamma^+_-(x^F_+,\Omega) \equiv \gamma^+_- = \hbar v^{x^F_+}_+ k_\alpha/(\hbar\Omega - 2\alpha k_\alpha x^F_+)$ with $\gamma^+_+ = \gamma^-_-$, as the velocities at the two bands are the same for a given Fermi energy. So, the final expression of intraband contribution $\chi^{0(1)}_{\rho\rho}(\mathbf{q},\omega)$ becomes

$$\begin{aligned}
\chi^{0(1)}_{\rho\rho}(\mathbf{q},\omega) = D_\alpha\sum_{\lambda=\lambda'}\frac{\left(x^F_{\lambda'}\right)^2}{\left|x^F_{\lambda'}+\lambda'\right|}\Bigg\{&(1+\lambda\lambda')\frac{1}{3}\left[Q\gamma^{\lambda'}_\lambda\left(x^F_{\lambda'},\Omega\right)\right]^2 + \lambda\lambda'\left(\frac{2\gamma^{\lambda'}_\lambda\left(x^F_{\lambda'},\Omega\right)}{15\left(x^F_{\lambda'}\right)^3} - \frac{\left[\gamma^{\lambda'}_\lambda\left(x^F_{\lambda'},\Omega\right)\right]^2}{15\left(x^F_{\lambda'}\right)^2}\right)Q^4\\
&+ (1+\lambda\lambda')\frac{1}{5}\left[Q\gamma^{\lambda'}_\lambda\left(x^F_{\lambda'},\Omega\right)\right]^4 + \lambda\lambda'\left(-\frac{2\left[\gamma^{\lambda'}_\lambda\left(x^F_{\lambda'},\Omega\right)\right]^2}{35\left(x^F_{\lambda'}\right)^4} + \frac{2\left[\gamma^{\lambda'}_\lambda\left(x^F_{\lambda'},\Omega\right)\right]^3}{35\left(x^F_{\lambda'}\right)^3} - \frac{\left[\gamma^{\lambda'}_\lambda\left(x^F_{\lambda'},\Omega\right)\right]^4}{35\left(x^F_{\lambda'}\right)^2}\right)Q^6\\
&+ (1+\lambda\lambda')\frac{1}{7}\left[Q\gamma^{\lambda'}_\lambda\left(x^F_{\lambda'},\Omega\right)\right]^6 + O(Q^8) + \cdots\Bigg\},
\end{aligned} \tag{B5}$$

and the final expression of one part of interband contribution $\chi^{0(2)}_{\rho\rho}(\mathbf{q},\omega)$ becomes

$$\chi^{0(2)}_{\rho\rho}(\mathbf{q},\omega) = D_\alpha \frac{(x^F_-)^2}{|x^F_- - 1|}\Bigg[\left(-\frac{2\gamma^-_+(x^F_-,\Omega)}{15(x^F_-)^3} + \frac{[\gamma^-_+(x^F_-,\Omega)]^2}{15(x^F_-)^2}\right)Q^4 + \left(\frac{2[\gamma^-_+(x^F_-,\Omega)]^2}{35(x^F_-)^4} - \frac{2[\gamma^-_+(x^F_-,\Omega)]^3}{35(x^F_-)^3} + \frac{[\gamma^-_+(x^F_-,\Omega)]^4}{35(x^F_-)^2}\right)Q^6 + O(Q^8) + \cdots\Bigg] + D_\alpha \frac{(x^F_+)^2}{|x^F_+ + 1|}\Bigg[\left(-\frac{2\gamma^+_-(x^F_+,\Omega)}{15(x^F_+)^3} + \frac{[\gamma^+_-(x^F_+,\Omega)]^2}{15(x^F_+)^2}\right)Q^4 + \left(\frac{2[\gamma^+_-(x^F_+,\Omega)]^2}{35(x^F_+)^4} - \frac{2[\gamma^+_-(x^F_+,\Omega)]^3}{35(x^F_+)^3} + \frac{[\gamma^+_-(x^F_+,\Omega)]^4}{35(x^F_+)^2}\right)Q^6 + \mathcal{O}(Q^8) + \cdots\Bigg]. \tag{B6}$$

The remaining part of the interband contribution $\chi^{0(3)}_{\rho\rho}(\mathbf{q},\omega)$ is finally given by

$$\begin{aligned}\chi^{0(3)}_{\rho\rho}(\mathbf{q},\omega) = D_\alpha \Bigg\{ & \frac{\xi_\alpha Q^2}{3\alpha k_\alpha}\left[\ln\left(\frac{(\hbar\Omega)^2 - (2\alpha k^F_+)^2}{(\hbar\Omega)^2 - (2\alpha k^F_-)^2}\right)\right] + \frac{8\xi^2_\alpha Q^4}{15}\left[\frac{1}{(\hbar\Omega)^2}\ln\left(\frac{4 - [\hbar\Omega/(\alpha k^F_+)]^2}{4 - [\hbar\Omega/(\alpha k^F_-)]^2}\right)\right. \\ & \left. - \frac{4\alpha k_\alpha (x^F_- - x^F_+)(x^F_- + x^F_+)(\hbar\Omega + 2\alpha k_\alpha)}{[(2\alpha k^F_-)^2 - (\hbar\Omega)^2][(2\alpha k^F_+)^2 - (\hbar\Omega)^2]}\right] + \frac{8\xi^3_\alpha Q^4}{15}\left[\frac{1}{(2\alpha k_\alpha)^3}\ln\left(\frac{(\hbar\Omega)^2 - (2\alpha k^F_+)^2}{(\hbar\Omega)^2 - (2\alpha k^F_-)^2}\right)\right. \\ & - \frac{1}{\{(2\alpha k_\alpha)^3[(\hbar\Omega)^2 - (2\alpha k^F_-)^2]^2[(\hbar\Omega)^2 - (2\alpha k^F_+)^2]^2\}}\left[4\alpha^2 k^2_\alpha (x^F_- - x^F_+)(x^F_- + x^F_+)(\hbar\Omega + 2\alpha k_\alpha)\right. \\ & \times \left[32\alpha^5 k^5_\alpha (x^F_- x^F_+)^2 + 80\alpha^4 k^4_\alpha \hbar\Omega (x^F_- x^F_+)^2 + 4\alpha^2 k^2_\alpha (\hbar\omega)^2[(x^F_+)^2 + (x^F_-)^2](2\alpha k_\alpha - 3\hbar\Omega)\right. \\ & \left.\left.\left. - 6\alpha k_\alpha (\hbar\Omega)^4 + (\hbar\Omega)^5\right]\right]\Bigg] + O(Q^6) + \cdots\Bigg\}. \end{aligned} \tag{B7}$$

Equations (B5), (B6), and (B7) combined to describe the asymptotic expression of the Lindhard function for $\xi_F > 0$.

Now we consider the Lindhard function for $\xi_F < 0$,

$$\begin{aligned}\chi^0_{\rho\rho}(\mathbf{q},\omega) &= \frac{1}{2\mathcal{V}}\sum_{\mathbf{k}}\left[1 + \frac{\mathbf{k}\cdot(\mathbf{k}+\mathbf{q})}{|\mathbf{k}||\mathbf{k}+\mathbf{q}|}\right]\frac{n^F_{\mathbf{k},-} - n^F_{\mathbf{k}+\mathbf{q},-}}{\hbar\Omega + \xi_{\mathbf{k},-} - \xi_{\mathbf{k}+\mathbf{q},-}} \\ &\quad + \frac{1}{2\mathcal{V}}\sum_{\mathbf{k}}\left[1 - \frac{\mathbf{k}\cdot(\mathbf{k}+\mathbf{q})}{|\mathbf{k}||\mathbf{k}+\mathbf{q}|}\right]\left[\frac{n^F_{\mathbf{k},-}}{\hbar\Omega + \xi_{\mathbf{k},-} - \xi_{\mathbf{k}+\mathbf{q},+}} - \frac{n^F_{\mathbf{k}+\mathbf{q},-}}{\hbar\Omega + \xi_{\mathbf{k},+} - \xi_{\mathbf{k}+\mathbf{q},-}}\right], \\ &= \frac{1}{2\mathcal{V}}\sum_{\mathbf{k}}\left[1 + \frac{\mathbf{k}\cdot(\mathbf{k}+\mathbf{q})}{|\mathbf{k}||\mathbf{k}+\mathbf{q}|}\right]\frac{\delta(\xi_{\mathbf{k},-} - \xi_F)\hbar v^k_- k_\alpha Q\cos\theta_{\mathbf{k}}}{\hbar\Omega - \hbar v^k_- k_\alpha Q\cos\theta_{\mathbf{k}}} \\ &\quad + \frac{1}{2\mathcal{V}}\sum_{\mathbf{k}}\left[1 - \frac{\mathbf{k}\cdot(\mathbf{k}+\mathbf{q})}{|\mathbf{k}||\mathbf{k}+\mathbf{q}|}\right]\frac{\delta(\xi_{\mathbf{k},-} - \xi_F)\hbar v^k_- k_\alpha Q\cos\theta_{\mathbf{k}}}{\hbar\Omega + 2\alpha k - \hbar v^k_- k_\alpha Q\cos\theta_{\mathbf{k}}} \\ &\quad + \frac{1}{2\mathcal{V}}\sum_{\mathbf{k}}\left[1 - \frac{\mathbf{k}\cdot(\mathbf{k}+\mathbf{q})}{|\mathbf{k}||\mathbf{k}+\mathbf{q}|}\right]\left[\frac{n^F_{\mathbf{k},-}}{\hbar\Omega - 2\alpha k - \hbar v^k_+ k_\alpha Q\cos\theta_{\mathbf{k}}} - \frac{n^F_{\mathbf{k},-}}{\hbar\Omega + 2\alpha k - \hbar v^k_- k_\alpha Q\cos\theta_{\mathbf{k}}}\right], \\ &= \chi^{0(1)}_{\rho\rho}(\mathbf{q},\omega) + \chi^{0(2)}_{\rho\rho}(\mathbf{q},\omega) + \chi^{0(3)}_{\rho\rho}(\mathbf{q},\omega). \end{aligned} \tag{B8}$$

Following the similar steps as in $\xi_F > 0$, the final expression for intraband $\lambda = \pm 1$ or intrabranch $\eta = 1, 2$ contribution to the Lindhard function is given by

$$\chi^{0(1)}_{\rho\rho}(\mathbf{q},\omega) = D_\alpha \sum_\eta \frac{\left(x^F_\eta\right)^2}{|x^F_\eta - 1|}\Bigg\{\frac{2}{3}\left[Q\gamma^-_-\left(x^F_\eta,\Omega\right)\right]^2 + \left(\frac{2\gamma^-_-\left(x^F_\eta,\Omega\right)}{15\left(x^F_\eta\right)^3} - \frac{\left[\gamma^-_-\left(x^F_\eta,\Omega\right)\right]^2}{15\left(x^F_\eta\right)^2}\right)Q^4 + \frac{2}{5}\left[Q\gamma^-_-\left(x^F_\eta,\Omega\right)\right]^4 + \left(-\frac{2\left[\gamma^-_-\left(x^F_\eta,\Omega\right)\right]^2}{35\left(x^F_\eta\right)^4} + \frac{2\left[\gamma^-_-\left(x^F_\eta,\Omega\right)\right]^3}{35\left(x^F_\eta\right)^3} - \frac{\left[\gamma^-_-\left(x^F_\eta,\Omega\right)\right]^4}{35\left(x^F_\eta\right)^2}\right)Q^6 + \frac{2}{7}\left[Q\gamma^-_-\left(x^F_\eta,\Omega\right)\right]^6 + O(Q^8) + \cdots\Bigg\}. \tag{B9}$$

with $x_\eta^F = k_\eta^F/k_\alpha$, and $\gamma_-^-(x_\eta^F, \Omega) = \xi_\alpha(x_\eta^F - 1)/(\hbar\Omega)$. The final expression of one part of interband and intrabranch contribution becomes

$$\chi_{\rho\rho}^{0(2)}(\mathbf{q},\omega) = D_\alpha \sum_\eta \frac{\left(x_\eta^F\right)^2}{|x_\eta^F - 1|}\left[\left(-\frac{2\gamma_+^-\left(x_\eta^F,\Omega\right)}{15\left(x_\eta^F\right)^3} + \frac{\left[\gamma_+^-\left(x_\eta^F,\Omega\right)\right]^2}{15\left(x_\eta^F\right)^2}\right)\mathcal{Q}^4 + \left(\frac{2\left[\gamma_+^-\left(x_\eta^F,\Omega\right)\right]^2}{35\left(x_\eta^F\right)^4} - \frac{2\left[\gamma_+^-\left(x_\eta^F,\Omega\right)\right]^3}{35\left(x_\eta^F\right)^3} + \frac{\left[\gamma_+^-\left(x_\eta^F,\Omega\right)\right]^4}{35\left(x_\eta^F\right)^2}\right)\mathcal{Q}^6 + O(\mathcal{Q}^8) + \cdots\right]. \tag{B10}$$

with $x_\eta^F = k_\eta^F/k_\alpha$ and $\gamma_+^-(x_\eta^F, \Omega) = \xi_\alpha(x_\eta^F - 1)/(\hbar\Omega + 2\alpha k_\alpha x_\eta^F)$. The remaining part of the intraband and intrabranch contribution to the Lindhard function has an expression similar to that of $\chi_{\rho\rho}^{0(3)}(\mathbf{q},\omega)$ for $\xi_F > 0$ except k_+^F is replaced k_1^F and k_-^F by k_2^F. So, the final expression of $\chi_{\rho\rho}^{0(3)}(\mathbf{q},\omega)$ for $\xi_F < 0$ becomes

$$\begin{aligned}\chi_{\rho\rho}^{0(3)}(\mathbf{q},\omega) = D_\alpha \Bigg\{ & \frac{\xi_\alpha \mathcal{Q}^2}{3\alpha k_\alpha}\left[\ln\left(\frac{(\hbar\Omega)^2 - \left(2\alpha k_1^F\right)^2}{(\hbar\Omega)^2 - \left(2\alpha k_2^F\right)^2}\right)\right] + \frac{8\xi_\alpha^2\mathcal{Q}^4}{15}\left[\frac{1}{(\hbar\Omega)^2}\ln\left(\frac{4 - \left[\hbar\Omega/\left(\alpha k_1^F\right)\right]^2}{4 - \left[\hbar\Omega/\left(\alpha k_2^F\right)\right]^2}\right)\right. \\ & \left. - \frac{4\alpha k_\alpha\left(x_2^F - x_1^F\right)\left(x_2^F + x_1^F\right)(\hbar\Omega + 2\alpha k_\alpha)}{\left[\left(2\alpha k_2^F\right)^2 - (\hbar\Omega)^2\right]\left[\left(2\alpha k_1^F\right)^2 - (\hbar\Omega)^2\right]}\right] + \frac{8\xi_\alpha^3\mathcal{Q}^4}{15}\left[\frac{1}{(2\alpha k_\alpha)^3}\ln\left(\frac{(\hbar\Omega)^2 - \left(2\alpha k_1^F\right)^2}{(\hbar\Omega)^2 - \left(2\alpha k_2^F\right)^2}\right)\right. \\ & - \frac{1}{\left\{(2\alpha k_\alpha)^3\left[(\hbar\Omega)^2 - \left(2\alpha k_2^F\right)^2\right]^2\left[(\hbar\Omega)^2 - \left(2\alpha k_1^F\right)^2\right]^2\right\}}\left[4\alpha^2 k_\alpha^2\left(x_2^F - x_1^F\right)\left(x_2^F + x_1^F\right)(\hbar\Omega + 2\alpha k_\alpha)\left[32\alpha^5 k_\alpha^5\left(x_2^F x_1^F\right)^2\right.\right. \\ & \left.\left. + 80\alpha^4 k_\alpha^4 \hbar\Omega\left(x_2^F x_1^F\right)^2 + 4\alpha^2 k_\alpha^2(\hbar\omega)^2\left[\left(x_2^F\right)^2 + \left(x_1^F\right)^2\right](2\alpha k_\alpha - 3\hbar\Omega) - 6\alpha k_\alpha(\hbar\Omega)^4 + (\hbar\Omega)^5\right]\right] + O(\mathcal{Q}^6) + \cdots\Bigg\}.\end{aligned} \tag{B11}$$

The full asymptotic expression of the Lindhard function for $\xi_F < 0$ is the sum of Eqs. (B9), (B10), and (B11).

APPENDIX C: DENSITY-DENSITY RESPONSE IN PRESENCE OF ELECTRON-ELECTRON INTERACTION

The Coulomb interaction among the band electrons in second quantized form can be written as follows [17,18]:

$$\hat{V} = \frac{1}{2}\sum_{\sigma,\sigma'}\int d\mathbf{r}\int d\mathbf{r}'\tilde{\Psi}_\sigma^\dagger(\mathbf{r})\tilde{\Psi}_{\sigma'}^\dagger(\mathbf{r}')\frac{e_0^2}{|\mathbf{r}' - \mathbf{r}|}\tilde{\Psi}_{\sigma'}(\mathbf{r}')\tilde{\Psi}_\sigma(\mathbf{r}), \tag{C1}$$

where $e_0^2 = e^2/(4\pi\epsilon)$, with ϵ being the background dielectric constant. After following the well-known procedure within the jellium model, the electron-electron interaction in second quantized form takes the following form in the helicity basis as

$$\hat{V} = \frac{1}{2\mathcal{V}}\sum_{\substack{\mathbf{k}_1,\mathbf{k}_2,\mathbf{q}'\neq 0\\ \lambda_1,\lambda_2,\lambda_3,\lambda_4}} V(q')C_{\mathbf{k}_1+\mathbf{q}',\lambda_1}^\dagger \phi_{\mathbf{k}_1+\mathbf{q}',\lambda_1}^\dagger C_{\mathbf{k}_2-\mathbf{q}',\lambda_2}^\dagger \phi_{\mathbf{k}_2-\mathbf{q}',\lambda_2}^\dagger \phi_{\mathbf{k}_2,\lambda_3} C_{\mathbf{k}_2,\lambda_3}\phi_{\mathbf{k}_1,\lambda_4} C_{\mathbf{k}_1,\lambda_4}, \tag{C2}$$

with $V(q') = 4\pi e_0^2/(q')^2$. In the presence of the elctron-electron interaction, the induced particle density due to the external perturbation defined above becomes

$$\rho_{\text{ind}}^i(\mathbf{r},t) = \int_{-\infty}^t dt'\int d\mathbf{r}'\chi_{\rho\rho}^i(\mathbf{r},\mathbf{r}',t,t')V_{\text{ext}}(\mathbf{r}',t'), \tag{C3}$$

where $\chi_{\rho\rho}^i(\mathbf{r},\mathbf{r}',t,t')$ is the retarded density-density response function for the system described by the total Hamiltonian $\hat{H} = \hat{H}_0 + \hat{V}$ and has following form:

$$\chi_{\rho\rho}^i(\mathbf{r},\mathbf{r}',t,t') = -\frac{i}{\hbar}\theta(t-t')\langle[\hat{\rho}(\mathbf{r},t),\hat{\rho}(\mathbf{r}',t')]\rangle_{\text{eq}}. \tag{C4}$$

Here the subscript $'\text{eq}'$ denotes that the average is taken over the ground state of the full Hamiltonian $\hat{H} = \hat{H}_0 + \hat{V}$ in equilibrium. Using the properties of the translationally invariant system even in the presence of the Coulomb interaction, the density response function takes the following form:

$$\chi_{\rho\rho}^i(\mathbf{q},t,t') = \sum_{\lambda\lambda'}\chi_{\lambda\lambda'}^i(\mathbf{q},t,t') = -\frac{i}{\hbar\mathcal{V}}\Theta(t-t')\langle[\hat{\rho}(\mathbf{q},t),\hat{\rho}(-\mathbf{q},t')]\rangle_{\text{eq}}. \tag{C5}$$

We use the standard equation of motion technique within the random phase approximation to obtain the final expression of the density-density response function of the interacting system, which is given by [17,18]

$$\chi^i_{\rho\rho}(\mathbf{q},\omega)=\sum_{\lambda\lambda'}\chi^i_{\lambda\lambda'}(\mathbf{q},\omega)=\frac{\chi^0_{\rho\rho}(\mathbf{q},\omega)}{1-V(\mathbf{q})\chi^0_{\rho\rho}(\mathbf{q},\omega)}, \tag{C6}$$

where $\chi^0_{\rho\rho}(\mathbf{q},\omega)$ is described by Eq. (A8). The plasmons are described by the poles of the above response function, i.e., zeros of the dielectric function $\epsilon(\mathbf{q},\omega)=1-V(\mathbf{q})\chi^0_{\rho\rho}(\mathbf{q},\omega)$.

APPENDIX D: OPTICAL CONDUCTIVITY

Let us first consider the NCMs without electron-electron interaction in the presence of an external perturbation, $\hat{V}_{\rm ext}(t)=\int d\mathbf{r}V_{\rm ext}(\mathbf{r},t)\hat{\rho}(\mathbf{r})$. The induced density due to this perturbation in Fourier space is given by [18]

$$\rho_{\rm ind}(\mathbf{q},\omega)=\chi^0_{\rho\rho}(\mathbf{q},\omega)V_{\rm ext}(\mathbf{q},\omega), \tag{D1}$$

with $\chi^0_{\rho\rho}(\mathbf{q},\omega)$ being the retarded density-density response for noninteracting NCMs. The continuity equation $\partial_t\rho_{\rm ind}(\mathbf{r},t)+\nabla\cdot\mathbf{J}(\mathbf{r},t)=0$ in Fourier space becomes $-i\omega\rho_{\rm ind}(\mathbf{q},\omega)+i\mathbf{q}\cdot\mathbf{J}(\mathbf{q},\omega)=0$, with the electrical current $\mathbf{J}(\mathbf{q},\omega)=\sigma(\mathbf{q},\omega)\mathbf{E}_{\rm ext}(\mathbf{q},\omega)$ in the presence of an external electric field $\mathbf{E}_{\rm ext}(\mathbf{q},\omega)=-i\mathbf{q}V_{\rm ext}(\mathbf{q},\omega)$. With the help of the above relations, the relation between the longitudinal conductivity $\sigma(\mathbf{q},\omega)$ and the dynamical polarization function $\chi^0_{\rho\rho}(\mathbf{q},\omega)$ is given by

$$\sigma(\mathbf{q},\omega)=\frac{i\omega e^2}{q^2}\chi^0_{\rho\rho}(\mathbf{q},\omega). \tag{D2}$$

In the presence of the electron-electron interaction, the above equations modify as follows:

$$\rho^i_{\rm ind}(\mathbf{q},\omega)=\chi^i_{\rho\rho}(\mathbf{q},\omega)V_{\rm ext}(\mathbf{q},\omega), \tag{D3}$$

where $\chi^i_{\rho\rho}(\mathbf{q},\omega)$ is the density response function for $\hat{H}=\hat{H}_0+\hat{V}$ with induced particle density $\rho^i_{\rm ind}(\mathbf{q},\omega)$ within RPA. The continuity equation is also modified in the same way as $-i\omega\rho^i_{\rm ind}(\mathbf{q},\omega)+i\mathbf{q}\cdot\mathbf{J}^i(\mathbf{q},\omega)=0$, giving rise to the following relation between $\sigma^i(\mathbf{q},\omega)$ and $\chi^i_{\rho\rho}(\mathbf{q},\omega)$:

$$\sigma^i(\mathbf{q},\omega)=\frac{i\omega e^2}{q^2}\chi^i_{\rho\rho}(\mathbf{q},\omega). \tag{D4}$$

[1] E. I. Rashba, Sov. Phys. Solid State **2**, 1109 (1960).
[2] Y. A. Bychkov and E. I. Rashba, J. Phys. C **17**, 6039 (1984).
[3] G. Dresselhaus, Phys. Rev. **100**, 580 (1955).
[4] S. A. Wolf, D. D. Awschalom, R. A. Buhrman, J. M. Daughton, S. von Molnar, M. L. Roukes, A. Y. Chtchelkanova, and D. M. Treger, Science **294**, 1488 (2001).
[5] R. Winkler, *Spin-Orbit Coupling Effects in Two-Dimensional Electron and Hole Systems* (Springer, Berlin, 2003).
[6] I. Zutic, J. Fabian, and S. Das Sarma, Rev. Mod. Phys. **76**, 323 (2004)
[7] S. Murakami, N. Nagaosa, and S. C. Zhang, Science **301**, 1348 (2003)
[8] S. Murakami, N. Nagaosa, and S. C. Zhang, Phys. Rev. B **69**, 235206 (2004)
[9] J. E. Hirsch, Phys. Rev. Lett. **83**, 1834 (1999).
[10] S. Zhang, Phys. Rev. Lett. **85**, 393 (2000).
[11] J. Sinova, D. Culcer, Q. Niu, N. A. Sinitsyn, T. Jungwirth, and A. H. MacDonald, Phys. Rev. Lett. **92**, 126603 (2004).
[12] Y. K. Kato, R. C. Myers, A. C. Gossard, and D. D. Awschalom, Science **306**, 1910 (2004)
[13] B. A. Bernevig and S. C. Zhang, Phys. Rev. Lett. **96**, 106802 (2006).
[14] J. Sinova, S. O. Valenzuela, J. Wunderlich, C. H. Back, and T. Jungwirth, Rev. Mod. Phys. **87**, 1213 (2015).
[15] K. Tsutsui and S. Murakami, Phys. Rev. B **86**, 115201 (2012).
[16] S. D. Ganichev, E. L. Ivchenko, V. V. Belkov, S. A. Tarasenko, M. Sollinger, D. Weiss, W. Wegscheider, and W. Prettl, Nature (London) **417**, 153 (2002).
[17] G. Giuliani and G. Vignale, *Quantum Theory of the Electron Liquid* (Cambridge University Press, Cambridge, UK, 2005).
[18] H. Bruus and K. Flensberg, *Many-Body Quantum Theory in Condensed Matter Physics: An Introduction* (Oxford University Press, Oxford, UK, 2004)
[19] G.-H. Chen and M. E. Raikh, Phys. Rev. B **59**, 5090 (1999).
[20] M. Pletyukhov and V. Gritsev, Phys. Rev. B **74**, 045307 (2006).
[21] D. K. Mukherjee, A. Kundu, and H. A. Fertig, Phys. Rev. B **98**, 184413 (2018).
[22] S. M. Badalyan, A. Matos-Abiague, G. Vignale, and J. Fabian, Phys. Rev. B **79**, 205305 (2009).
[23] A. Scholz, T. Dollinger, P. Wenk, K. Richter, and J. Schliemann, Phys. Rev. B **87**, 085321 (2013).
[24] X. F. Wang, Phys. Rev. B **72**, 085317 (2005).
[25] M. Bianchi, D. Guan, S. Bao, J. Mi, B. B. Iversen, P. D. C. King, and P. Hofmann, Nat. Commun. **1**, 128 (2010).
[26] P. D. C. King, R. C. Hatch, M. Bianchi, R. Ovsyannikov, C. Lupulescu, G. Landolt, B. Slomski, J. H. Dil, D. Guan, J. L. Mi, E. D. L. Rienks, J. Fink, A. Lindblad, S. Svensson, S. Bao, G. Balakrishnan, B. B. Iversen, J. Osterwalder, W. Eberhardt,

F. Baumberger, and P. Hofmann, Phys. Rev. Lett. **107**, 096802 (2011).
[27] C. R. Ast, J. Henk, A. Ernst, L. Moreschini, M. C. Falub, D. Pacile, P. Bruno, K. Kern, and M. Grioni, Phys. Rev. Lett. **98**, 186807 (2007).
[28] K. Ishizaka, M. S. Bahramy, H. Murakawa, M. Sakano, T. Shimojima, T. Sonobe, K. Koizumi, S. Shin, H. Miyahara, A. Kimura, K. Miyamoto, T. Okuda, H. Namatame, M. Taniguchi, R. Arita, N. Nagaosa, K. Kobayashi, Y. Murakami, R. Kumai, Y. Kaneko, Y. Onose, and Y. Tokura, Nat. Mater. **10**, 521 (2011).
[29] M. S. Bahramy, R. Arita, and N. Nagaosa, Phys. Rev. B **84**, 041202(R) (2011).
[30] S. V. Eremeev, I. A. Nechaev, Y. M. Koroteev, P. M. Echenique, and E. V. Chulkov, Phys. Rev. Lett. **108**, 246802 (2012).
[31] G. Landolt, S. V. Eremeev, Y. M. Koroteev, B. Slomski, S. Muff, T. Neupert, M. Kobayashi, V. N. Strocov, T. Schmitt, Z. S. Aliev, M. B. Babanly, I. R. Amiraslanov, E. V. Chulkov, J. Osterwalder, and J. H. Dil, Phys. Rev. Lett. **109**, 116403 (2012).
[32] M. Sakano, M. S. Bahramy, A. Katayama, T. Shimojima, H. Murakawa, Y. Kaneko, W. Malaeb, S. Shin, K. Ono, H. Kumigashira, R. Arita, N. Nagaosa, H. Y. Hwang, Y. Tokura, and K. Ishizaka, Phys. Rev. Lett. **110**, 107204 (2013).
[33] J. Kang and J. Zang, Phys. Rev. B **91**, 134401 (2015).
[34] V. P. Mineev and Y. Yoshioka, Phys. Rev. B **81**, 094525 (2010).
[35] I. I. Boiko and E. I. Rashba, Fiz. Tverd. Tela (Leningrad) **2**, 1874 (1960) [Sov. Phys. Solid State **2**, 1692 (1960)].
[36] G. A. H. Schober, H. Murakawa, M. S. Bahramy, R. Arita, Y. Kaneko, Y. Tokura, and N. Nagaosa, Phys. Rev. Lett. **108**, 247208 (2012).
[37] H. Murakawa, M. S. Bahramy, M. Tokunaga, Y. Kohama, C. Bell, Y. Kaneko, N. Nagaosa, H. Y. Hwang, and Y. Tokura, Science **342**, 1490 (2013).
[38] C. Bell, M. S. Bahramy, H. Murakawa, J. G. Checkelsky, R. Arita, Y. Kaneko, Y. Onose, M. Tokunaga, Y. Kohama, N. Nagaosa, Y. Tokura, and H. Y. Hwang, Phys. Rev. B **87**, 081109(R) (2013).
[39] C. Martin, E. D. Mun, H. Berger, V. S. Zapf, and D. B. Tanner, Phys. Rev. B **87**, 041104(R) (2013).
[40] T. Ideue, J. G. Checkelsky, M. S. Bahramy, H. Murakawa, Y. Kaneko, N. Nagaosa, and Y. Tokura, Phys. Rev. B **90**, 161107(R) (2014).
[41] L. Ye, J. G. Checkelsky, F. Kagawa, and Y. Tokura, Phys. Rev. B **91**, 201104(R) (2015).
[42] C. R. Wang, J. C. Tung, R. Sankar, C. T. Hsieh, Y. Y. Chien, G. Y. Guo, F. C. Chou, and W. L. Lee, Phys. Rev. B **88**, 081104(R) (2013).
[43] V. Brosco and C. Grimaldi, Phys. Rev. B **95**, 195164 (2017).
[44] N. Ogawa, M. S. Bahramy, H. Murakawa, Y. Kaneko, and Y. Tokura, Phys. Rev. B **88**, 035130 (2013).
[45] S. Maiti, V. Zyuzin, and D. L. Maslov, Phys. Rev. B **91**, 035106 (2015).
[46] P. Di Pietro, F. M. Vitucci, D. Nicoletti, L. Baldassarre, P. Calvani, R. Cava, Y. S. Hor, U. Schade, and S. Lupi, Phys. Rev. B **86**, 045439 (2012).
[47] L. Wu, J. Yang, S. Wang, P. Wei, J. Yang, W. Zhang, and L. Chen, Phys. Rev. B **90**, 195210 (2014).
[48] T. Ideue, L. Ye, J. G. Checkelsky, H. Murakawa, Y. Kaneko, and Y. Tokura, Phys. Rev. B **92**, 115144 (2015).
[49] S. X. Wang, H. R. Chang, and J. Zhou, Phys. Rev. B **96**, 115204 (2017).
[50] K. Togano, P. Badica, Y. Nakamori, S. Orimo, H. Takeya, and K. Hirata, Phys. Rev. Lett. **93**, 247004 (2004).
[51] M. Smidman, M. B. Salamon, H. Q. Yuan, and D. F. Agterber, Rep. Prog. Phys. **80**, 036501 (2017).
[52] K. V. Samokhin, Phys. Rev. B **78**, 144511 (2008).
[53] V. P. Mineev, Phys. Rev. B **88**, 134514 (2013).
[54] K. V. Samokhin, Phys. Rev. B **76**, 094516 (2007).
[55] S. Verma, T. Biswas, and T. K. Ghosh, Phys. Rev. B **100**, 045201 (2019).
[56] K.-W. Lee and W. E. Pickett, Phys. Rev. B **72**, 174505 (2005).
[57] S. Dey and R. Sensarma, Phys. Rev. B **94**, 235107 (2016).
[58] X. Xi, C. Ma, Z. Liu, Z. Chen, W. Ku, H. Berger, C. Martin, D. B. Tanner, and G. L. Carr, Phys. Rev. Lett. **111**, 155701 (2013).